JGR Oceans

RESEARCH ARTICLE
10.1029/2018JC014804

A Review of Wave Spectrum Models as Applied to the Problem of Radar Probing of the Sea Surface

M. Ryabkova[1], V. Karaev[1], J. Guo[2,3,4], and Yu. Titchenko[1]

[1]Institute of Applied Physics of the Russian Academy of Sciences, Nizhny Novgorod, Russia, [2]CAS Key Laboratory of Coastal Environmental Processes and Ecological Remediation, Yantai Institute of Coastal Zone Research, Chinese Academy of Sciences, Yantai, China, [3]Center for Ocean Mega-Science, Chinese Academy of Sciences, Quindao, China, [4]Shandong Key Laboratory of Coastal Environmental Processes, Yantai Institute of Coastal Zone Research, Chinese Academy of Sciences, Yantai, China

Abstract The most common models of the wind wave spectrum are reviewed, and the compliance of the studied spectra with several fundamental criteria is estimated. These criteria are the ability to simulate diverse wave climate and agreement between model-based calculations of the mean square slope and experimental data. The spreading function of the spectrum should also correspond to the experimentally measured Doppler spectrum, while the dependence of the radar backscatter cross section should conform to geophysical model functions for various wavelength ranges of incident electromagnetic radiation at moderate incidence angles (20–60°). An analysis has shown that none of the considered spectrum models fully satisfies all the criteria; thus, a new spectrum model for wind waves was developed. Boundary wave numbers for various wavelength ranges of incident electromagnetic radiation within the framework of a two-scale surface model were determined for the new model. The spectrum model can be used to simulate ripple attenuation in oil slicks and to calculate the radar backscatter cross section inside slick.

Plain Language Summary Wave frequency spectra describe the distribution of wave energy over wave frequencies. They are used for numerical simulation of the sea surface. There are a lot of measurements of wind-generated gravity waves spectrum; as for waves of smaller wavelengths, they are more difficult to measure in field experiments, while laboratory experiments do not show the same statistics as an actual sea. To combine the available in situ and laboratory measurements of spectra in various wavelength ranges, researchers have developed a variety of models of the wave spectrum; each model is aimed at solving a specific problem. In this paper, we make a comparative analysis of the spectrum models developed by T. Elfouhaily, P. A. Hwang, V. N. Kudryavtsev, and V. Yu. Karaev with their coauthors and present a new spectrum model that eliminates some drawbacks inherent in other models. It should be emphasized that the new wave spectrum model is not a complete and precise oceanographic description of waves. The aim of our work is to develop a wave spectrum model, which is based on known oceanographic and radar data and can be used for numerical estimates in studying microwave electromagnetic wave scattering from the sea surface.

Key Points:
- A comparative analysis of the spectrum models developed by Elfouhaily, Hwang, Kudryavtsev, and Karaev with their coauthors was made
- Karaev spectrum model was modified on the basis of the gravity-capillary waves field measurements
- The advantage of the modified spectrum more adequately describes MSS and the RCS than other models and is convenient for use

Supporting Information:
- Supporting Information S1

Correspondence to:
J. Guo and M. Ryabkova,
jguo@yic.ac.cn;
m.rjabkova@gmail.com

Citation:
Ryabkova, M., Karaev, V., Guo, J., & Titchenko, Yu. (2019). A review of wave spectrum models as applied to the problem of radar probing of the sea surface. *Journal of Geophysical Research: Oceans*, *124*, 7104–7134. https://doi.org/10.1029/2018JC014804

Received 23 NOV 2018
Accepted 13 SEP 2019
Accepted article online 1 OCT 2019
Published online 23 OCT 2019

1. Introduction

Models of the wave spectrum are widely used to simulate the sea surface in estimating prospects of new algorithms for radar data processing, schemes of measurement, and development of new radars.

Sea waves always provoked interest of researchers but were quantitatively described only recently, and the first reliable wave spectra were obtained in the mid-1960s (Kitaigorodskii, 1962; Pierson & Moskowitz, 1964). Models of the sea wave spectrum were developed due to computer engineering progress, since it enabled one to handle large data sets.

Unfortunately, the wave spectra developed by the oceanographers do not fully meet the requirements set by remote sensing specialists. The spectra used for solving radar probing problems should describe a wide range of wavelengths, namely, from several hundred meters to several millimeters, because electromagnetic wave scattering is affected by both short and long waves. No field experiments have been carried out so far, in which the entire wavelength range has been measured simultaneously. Accordingly, there is no generally recognized model of the wave spectrum covering the entire wavelength range. Scientists involved in

remote sensing needed such a wave spectrum; thus, they participated in developing wave spectra covering the entire wavelength range and proposed their models of spectra. To combine the available in situ and laboratory measurements of spectra in various wavelength ranges, researchers have developed a variety of wave spectrum models, each of which is aimed at solving a specific problem (Apel, 1994; Bjerkaas & Riedel, 1979; Bringer et al., 2014; Cheng et al., 2006; Donelan & Pierson, 1987; Elfouhaily et al., 1997; Fois et al., 2014; Hasselmann et al., 1973; Hwang & Fois, 2015a; Kudryavtsev et al., 1999, 2003, 2005; Plant, 2002; Toba, 1973; Yurovskaya et al., 2013; Zakharov & Zaslavsky, 1982).

In this paper, we make a comparative analysis of the most popular wave spectrum models to solve remote sensing problems (the models developed by T. Elfouhaily with coauthors (Elfouhaily et al., 1997), P. A. Hwang with coauthors (Hwang & Fois, 2015a), and V. N. Kudryavtsev with coauthors (the last version of the spectrum model is presented in Appendix A in Yurovskaya et al., 2013) and the spectrum model developed by V. Yu. Karaev with coauthors (Karaev et al., 2008; Karaev & Balandina, 2000) and present a new spectrum model that eliminates some drawbacks inherent in other models. Comparison of the theoretical estimates obtained from the new wave spectrum with the experimental data has shown that they are in fairly good agreement.

It should be emphasized that the new model of the wave spectrum cannot be considered as a complete and precise oceanographic description of waves. To construct such a spectrum, extensive oceanographic studies are needed. The aim of our work is to develop a spectrum model for sea waves, which is based on known oceanographic and radar data and can be used for numerical estimates in studying microwave electromagnetic wave scattering from the sea surface.

In our opinion, an important factor is the convenient use of the spectrum model. We tried to simplify the formula of the spectrum for using it in analytic transformations, for example, in integration. This spectrum can be conventionally called the "radiophysical" one. The advantage of the developed wave spectrum model compared to the previous ones is that it is more adequately describes some effects observed in radar probing of the ocean and is convenient for use.

The second section of the paper presents a brief history of developing the wind wave spectrum models, which were applied and are being applied for modeling in remote sensing problems. Several relatively new spectrum models are selected for the analysis, since they are not only widely used by researchers for modeling but also represent different approaches to the construction of the wave spectrum model. These spectrum models are described in the third section, while the fourth section deals with comparison of the models by several criteria that the authors consider essential for the spectrum used for modeling in remote sensing problems. Since none of the examined spectrum models meets all the requirements, a new spectrum model has been developed. The new model of the wave spectrum is presented in the fifth section. Boundary wave numbers for various wavelength ranges of incident electromagnetic radiation within the framework of a two-scale surface model were determined for the new spectrum model. The full spectrum (including swell) is described in the sixth section. The terminology used in the paper is presented and explained in Appendix A.

2. Brief Historical Review

This paper will introduce a comparative analysis of the most popular wave spectrum models to solve remote sensing problems (presented in section 3). The historical review mainly focuses on works that provided data for those spectrum models.

The first spectra of surface waves that appeared in the 1950–1960s of the twentieth century described fully developed wind waves, that is, waves driven by permanent and homogeneous wind, which blew for such a long time and at such a large fetch that a balance was reached between input and dissipated energies for all wavelengths in the spectrum and the wave spectrum parameters did not vary with further increase in the fetch length. A fully developed wind wave is an idealistic concept, it is widely used but unreal (Alves et al., 2003), while the most common case is mixed seas when swell is present on the sea surface together with wind waves.

The formula for the wave spectrum was proposed in (Pierson & Moskowitz, 1964)

$$S(\omega) = \frac{\alpha g^2}{\omega^5} e^{-\beta\left(\frac{\omega_{\max}}{\omega}\right)^4}. \quad (1)$$

This formula was obtained as a result of developing the similarity theory and the consequent idea formulated by Kitaigorodskii (1962) that elevation spectra of fully developed wind waves represented in dimensionless coordinates have similar shapes at all wind speeds. By analyzing the measured elevation spectra converted to dimensionless coordinates, Pierson and Moskowitz (1964) obtained an analytic formula for the spectrum of equation (1) with the coefficients $\alpha = 8.10 \cdot 10^{-3}$,$\beta = 0.74$. $\omega_{\max} = \frac{g}{U_{19}}$ is the spectral maximum, where g is the acceleration due to gravity and U_{19} is the wind speed at a height of 19.5 m above the sea surface.

The paper (Hasselmann et al., 1973) is devoted to the results of the major international experiment Joint North Sea Wave Project (JONSWAP). The measurements covered the cases of developing wind waves, and it turned out that the spectral densities at the frequency $\omega_{\max}$ were several times higher than spectrum approximations (1). To describe this effect, the peakedness of the spectrum γ, that is, the ratio of the base maximum of the spectrum to its approximation value (1) at the same frequency $\omega_{\max}$, was introduced into the formula

$$S(\omega) = \frac{ag^2}{\omega^5}(2\pi)e^{-1.25\left(\frac{\omega_{\max}}{\omega}\right)^4}\gamma^{\exp\left[-\frac{(\omega-\omega_{\max})^2}{2\sigma^2\omega_{\max}^2}\right]}, \quad (2)$$

$$\sigma = \begin{cases} \sigma_a, \omega \le \omega_{\max}, \\ \sigma_b, \omega > \omega_{\max}. \end{cases}$$

The developing waves are described by the dimensionless wave fetch $\widetilde{x}$ and the dimensionless frequency $\widetilde{\omega}$:

$$\widetilde{x} = \frac{xg}{U_{10}^2}, \quad (3a)$$

$$\widetilde{\omega} = \frac{\omega \cdot U_{10}}{g}, \quad (3b)$$

where x is the wave fetch in meters. If waves develop from the coast under the influence of wind, the fetch length coincides with the distance to the coast. $\omega_{\max}$ is an adjustable parameter in the JONSWAP spectrum. The dependence of $\widetilde{\omega}_{\max}$, α, σ_a, σ_b, and γ on dimensionless fetch was found (Hasselmann et al., 1973). The spectrum of equation (2) is widely used for wave modeling in the range near the spectral peak.

In the wave number domain, the JONSWAP spectrum is expressed as follows (Young, 1999):

$$S(\omega) = 4\pi^2 \frac{\alpha}{2k^3} e^{-1.25\left(\frac{k_p}{k}\right)^4} \gamma^{\exp\left[-\frac{(k-k_p)^2}{2\sigma^2 k_p^2}\right]}, \quad (4)$$

where $k_p = \omega_{\max}^2/g$ is the wave number corresponding to the spectral peak $\omega_{\max}$ (Plant, 2009). The dispersion relation (A1) is valid for the case of deep water, while near the spectral peak, it transforms into $\omega^2 = gk$.

The equilibrium range is behind the spectral peak area. The concept of an equilibrium range was introduced by Phillips (1958). Proceeding from the similarity theory, Phillips proposed the following approximation of the equilibrium range of the frequency spectrum:

$$S(\omega) = \frac{\alpha g^2}{\omega^5}, \quad (5)$$

where α is the Phillips constant. Approximation (5) was obtained by Phillips on the assumption that the limiting configuration of the wave surface (if crests are not blown away by wind) and, hence, the energy in the equilibrium range of the spectrum are determined by the acceleration limit of liquid particles, which is proportional to the acceleration due to gravity g, the air density ρ_a, the water density ρ_w, and the frequency ω. The Phillips approximation for the equilibrium range was confirmed by a series of field experiments (Banner, 1990; Hasselmann et al., 1973), but the boundaries of the equilibrium range depend on the wind speed and the degree of wind wave development; the researchers' opinions are divided on this point.

Phillips (1958) introduced rather broad boundaries of the equilibrium range: $\omega_0 \ll \omega \ll \sqrt[4]{\frac{4\rho_w g^3}{T}}$, $k_0 \ll k \ll \sqrt{\frac{\rho_w g}{T}}$, where the lower limits of ω_0 and k_0 are the lowest frequency and the corresponding wave number, starting from which the nonlinear wave interactions significantly affect the spectrum, while the upper limit is associated with a transition to the capillary range of the spectrum; here T is the surface tension coefficient of water.

The problem of verifying the Phillips hypothesis and refining the coefficient α and the exponent -5 in the dependence on ω based on experimental data is considered in detail in Davidan et al. (1985). Davidan limits the equilibrium interval from below by $\omega_{p1} = 2\omega_{\max}\widetilde{\omega}_{\max}^{-0.7}$ for $\widetilde{\omega}_{\max} < 2.4$ and from above by the inequality $\omega > 5\omega_{\max}$.

A number of theoretical and experimental studies (Kitaigorodskii, 1962; Kitaigorodskii et al., 1975; Kahma, 1981; Phillips, 1985; Toba, 1973; Zakharov & Filonenko, 1996) support the approximation of the equilibrium spectrum of the form

$$S(\omega) \propto \omega^{-4}. \tag{6}$$

As an exact isotropic stationary solution of the kinetic equation, Zakharov and Zaslavsky (1982) obtained the approximation of the spectrum on its descending branch

$$S(\omega) \propto \omega^{-11/3}. \tag{7}$$

The dependence of the descending branch of the spectrum in a range from ω^{-3} to ω^{-5} for different approximations of the kinetic equation is shown in Kitaigorodskii et al. (1975). Liu (1989) analyzed the spectra measured by National Data Buoy Center buoys installed in the Great Lakes. Figure 8 from Liu (1989) shows the distribution of exponents of spectral slopes: Most of them are in the range from -3 to -7 with the peak between -4 and -5. The problem of correct approximation for the equilibrium part of the spectrum is still unsolved. There are a number of studies on this subject (Liu, 1989; Rodrigues & Soares, 1999; Young, 1999; Zakharov & Badulin, 2015).

3. Review of Wave Spectrum Models

To solve the problems of radar probing of the sea surface, it is needed to have a wave spectrum valid over the range from hundreds of meters to millimeters. The abovementioned models of spectra correctly describe only the gravity waves. Therefore, it became necessary to develop a wave spectrum for the entire wavelength range.

We will review three popular models of the sea wave spectrum, which are frequently used to obtain numerical estimates in remote sensing problems: the models developed by T. Elfouhaily with coauthors (Elfouhaily et al., 1997), P. A. Hwang with coauthors (Hwang & Fois, 2015a), and V. N. Kudryavtsev with coauthors (last version of the spectrum model is presented in Appendix A in Yurovskaya et al., 2013) as well as the wave spectrum model developed by V. Yu. Karaev with coauthors (Karaev et al., 2008; Karaev & Balandina, 2000), which is used by our team to model large-scale waves and calculate the spectral and energy characteristics of a scattered radar microwave signal within the framework of a two-scale model of the scattering surface. The wave spectrum previously showed a good agreement between the modeling results and experimental data in processing of altimetric measurements (Karaev et al., 2002).

The development of the first Russian scatterometer (Karaev et al., 2015) required modeling of the electromagnetic wave scattering from the sea surface at moderate incidence angles. It has been found that in the gravity-capillary range, the Karaev spectrum does not agree with the experimental data, which leads to errors in model data processing. Thus, it was necessary to choose a wave spectrum from the known models or to refine the available wave spectrum model in the gravity-capillary wave range. Such a refinement procedure was carried out with the Kudryavtsev et al. (2005) spectrum, in which the gravity-capillary part of the spectrum was also improved on the basis of new experimental data in 2013 (Yurovskaya et al., 2013).

The criteria for choosing a model and comparing models of wave spectra are given in the next section. It should be noted that the analyzed models not only are the most frequently used ones but also implement radically different approaches to the construction of the sea wave spectrum throughout the wavelength range. The recently published versions of the spectra were used for the modeling.

3.1. V. Yu. Karaev spectrum

The V. Yu. Karaev model was first published as a preprint in 1998 (Karaev et al., 1998), the Russian version of the paper was published in 2000 (Karaev & Balandina, 2000), and the English version was published in 2008 (Karaev et al., 2008). The development of a wave spectrum model covering all wavelengths was motivated at that time by the absence of a wave model that could be used to solve the direct and inverse problems of radar probing of the sea surface.

The wave spectrum models known at that time did not cover the entire range of wavelengths that were important for solving radar probing problems (from hundreds of meters to millimeters), and there was no spectrum model that satisfactorily described the known experimental data; thus, it was decided to develop a new spectrum model. The model was designed to study backscattering at small incidence angles (quasi-specular scattering within the framework of a two-scale model of sea surface), and special attention was paid to the low-frequency part of the sea wave spectrum.

In the range near the spectral peak, the spectrum obtained in the large international JONSWAP experiment (Hasselmann et al., 1973; equation (2) in section 2) is generally accepted.

In Hasselmann et al. (1973), a change in the spectrum peakedness parameter γ with a variation in the dimensionless wave fetch is observed, but no unambiguous relationship between them is found. The average value of γ is estimated at 3.3. When analyzing the dependence of γ on the stage of wave development (Karaev & Balandina, 2000), the data of the JONSWAP experiment and experiments made in the seas and inland waters of the Union of Soviet Socialist Republics were used (Davidan et al., 1985). It was shown that the peakedness parameter γ decreased with the wave development (Davidan et al., 1985). Using the data given in Davidan (1983) and the experimental data from Ewing (1980), the dependences of the parameters α, γ, and $\widetilde{\omega}_m$ on the degree of wave development and on the wind speed were determined (Karaev et al., 2008; Karaev & Balandina, 2000):

$$\widetilde{\omega}_m = 0.61826 + 0.000003529\widetilde{x} - 0.00197508\sqrt{\widetilde{x}} + \frac{62.554}{\sqrt{\widetilde{x}}} - \frac{290.2}{\widetilde{x}}, \tag{8a}$$

$$\gamma = 5.25366 + 0.000107622\widetilde{x} - 0.03776776\sqrt{\widetilde{x}} - \frac{162.9835}{\sqrt{\widetilde{x}}} + \frac{253251.5}{\widetilde{x}^{1.5}}, \tag{8b}$$

$$\alpha = 0.0311937 - 0.002327736 ln(\widetilde{x}) - \frac{8367.9}{\widetilde{x}^2} + 4.51146 \cdot e^{\left(1420-\widetilde{x}\right)}. \tag{8c}$$

Estimates of the parameters α, γ, and $\widetilde{\omega}_m$ are also discussed in Kanevsky (2017)). The dependence of the wave integral parameters on the wave generation conditions is reviewed in Babanin and Soloviev (1998)).

As it was mentioned in section 2, in the gravity wave range directly behind the spectral peak, there is an equilibrium range, where the dependence of the spectrum on the frequency is proportional to ω^{-4} (Kahma, 1981; Kitaigorodskii, 1962; Phillips, 1985; Toba, 1973; Zakharov & Filonenko, 1996). Numerous experimental studies have shown that there is a secondary peak of the spectral density in the gravity-capillary range (Hwang et al., 1996; Jähne & Riemer, 1990).

Knowledge of the pattern of change in the wave spectral density in a wide range of wavelengths allowed V. Yu. Karaev to construct a "radiophysical" wave spectrum of the form (Karaev et al., 2008; Karaev & Balandina, 2000):

$$S_{\sum}(\omega) = S_{\xi}(\omega), \quad 0<\omega<1.2\omega_m, \tag{9a}$$

$$S_{\sum}(\omega) = \frac{\alpha_2}{\omega^4}, \quad 1.2\omega_m<\omega<a_m\omega_m, \tag{9b}$$

$$S_{\sum}(\omega) = \frac{\alpha_3}{\omega^5}, \quad a_m\omega_m<\omega<\omega_{gc}\approx 64\frac{\text{rad}}{\text{s}}, \left(k_{gc} = 270\frac{\text{rad}}{\text{m}}\right), \tag{9c}$$

$$S_{\sum}(\omega) = \frac{\alpha_4}{\omega^{2.7}}, \quad \omega_{gc}<\omega<\omega_c\approx 298\frac{\text{rad}}{\text{s}}, \left(k_c = 1020\frac{\text{rad}}{\text{m}}\right), \tag{9d}$$

$$S_{\sum}(\omega) = \frac{\alpha_5}{\omega^5}, \quad \omega_c < \omega. \tag{9e}$$

Here $S_\xi(\omega)$ is the JONSWAP spectrum (equation (2) in section 2), while the coefficients α_i are calculated as

$$\alpha_2 = S_{\sum}(1.2\omega_m)\cdot(1.2\omega_m)^4, \tag{10a}$$

$$\alpha_3 = \alpha_2 \cdot a_m \omega_m, \tag{10b}$$

$$\alpha_4 = \frac{\alpha_3}{\omega_{gc}^{2.3}}, \tag{10c}$$

$$\alpha_5 = \alpha_4 \cdot \omega_{gc}^{2.3}. \tag{10d}$$

The coefficient a_m depends on the wind speed and is given by

$$a_m = 0.3713 + 0.29024U_{10} + \frac{0.2902}{U_{10}}. \tag{11}$$

Based on the angular distribution model developed by Banner (1990), the formula for the angular distribution is proposed

$$\Phi_\omega = A \cdot \frac{2}{e^{2B\varphi} + e^{-2B\varphi}}, -\pi \le \varphi \le \pi, \tag{12}$$

where $B = 10^b$, φ is the angle between the probing and wave propagation directions, and

$$b = -0.28 + 0.65 \cdot exp\left[-0.75 \cdot ln\left(\frac{k}{k_p}\right)\right] + 0.01 \cdot exp\left[-0.2 + 0.7 \cdot lg\left(\frac{k}{k_p}\right)\right]. \tag{13}$$

The normalization coefficient is represented as

$$A = \frac{B}{arctan(sh2\pi B)}. \tag{14}$$

It is assumed that the model of the wind wave spectrum is valid at wind speeds from 2.5 to 22 m/s and dimensionless wind fetches $\widetilde{x}$ from 1,430 to 20,170, where the dimensionless wind fetch $\widetilde{x} = 20{,}170$ corresponds to fully developed wind waves. These constraints follow from the conditions of the experiments on which the authors relied.

Figure 1 shows the elevation and curvature spectra (defined in equations (A2) and (A7), respectively) of the Karaev's spectrum model at a wind speed of $U_{10} = 10$ m/s for various wind fetch lengths.

Figure 2 shows the spectra of elevations and spectra of curvatures of the Karaev's spectrum model for fully developed waves ($\widetilde{x} = 20{,}170$) for various wind speeds.

Karaev's spectrum model (Karaev et al., 2008; Karaev & Balandina, 2000) is referred in this paper as Karaev2000.

3.2. T. Elfouhaily Spectrum

Elfouhaily et al. (1997) analyzed models of wave spectrum for long- and short-wavelength parts of the spectrum, widely used at that time. The drawbacks of these spectra were noted, in particular, the discrepancy with the Cox and Munk (1954) experiments and the nonanalytic form of the functions of the spectra. The authors have developed a new spectrum model aimed at solving the problems of radar probing of the sea surface.

The omnidirectional spectrum of curvatures was given as the sum of long- and short-wavelength parts

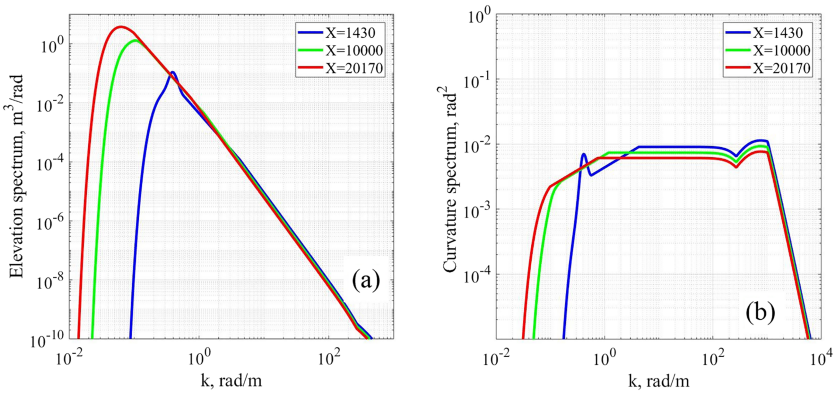

Figure 1. Elevation spectra (a) and curvature spectra (b) of developing wind waves according to the V. Yu. Karaev spectrum model. The wind speed is $U_{10} = 10$ m/s, and the dimensionless wind fetches are $\tilde{x} = 1{,}430$ (blue curve), 10,000 (green curve), and 20,170 (red curve).

$$S(k) = \frac{B_l + B_h}{k^3}, \tag{15}$$

where subscripts "l" and "h" denote low and high frequencies, respectively. The transition between long- and short-wavelength parts of the spectrum is described by exponential factor in B_l:

$$F_p = exp\left\{-\frac{\Omega}{\sqrt{10}}\left[\sqrt{\frac{k}{k_p}}-1\right]\right\}, \tag{16}$$

where Ω is the inverse wave age. The exponential factor limits the energy of waves with $k > 10k_p$. Such a cut-off point was introduced on the basis of Klinke and Jähne (1992) laboratory experiments.

The degree of wind wave development is determined by the inverse wave age Ω. The dependence of the inverse wave age on the dimensionless wind fetch is given by

$$\Omega = 0.84 \cdot \tanh^{-0.75}\left\{\left(\frac{\tilde{x}}{x_0}\right)^{0.4}\right\}, x_0 = 2.2 \cdot 10^4. \tag{17}$$

Here U_{10} is the wind speed at a height of 10 m above the surface. Fully developed wind waves correspond to $\Omega = 0.84$ ($\tilde{x} \to \infty$). The wave age $\Omega = 2$ corresponds to dimensionless fetch $\tilde{x} = 1{,}430$.

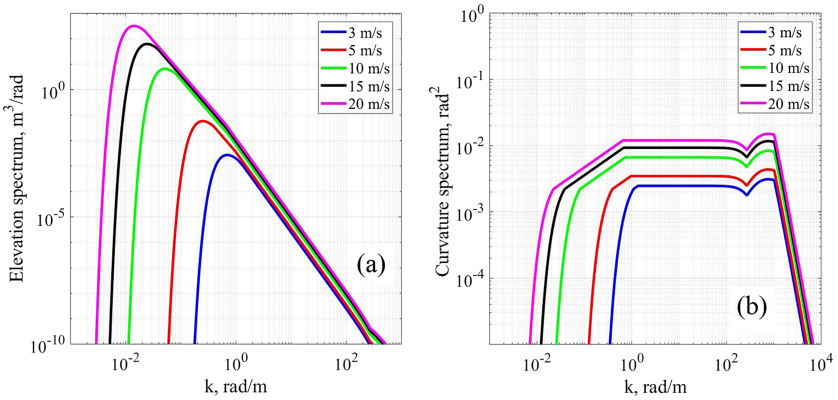

Figure 2. Spectra of elevations (a) and spectra of curvatures (b) of the V. Yu. Karaev spectrum model for fully developed waves. The dark blue curve denotes $U_{10} = 3$ m/s, red $U_{10} = 5$ m/s, green $U_{10} = 10$ m/s, black $U_{10} = 15$ m/s, and purple $U_{10} = 20$ m/s.

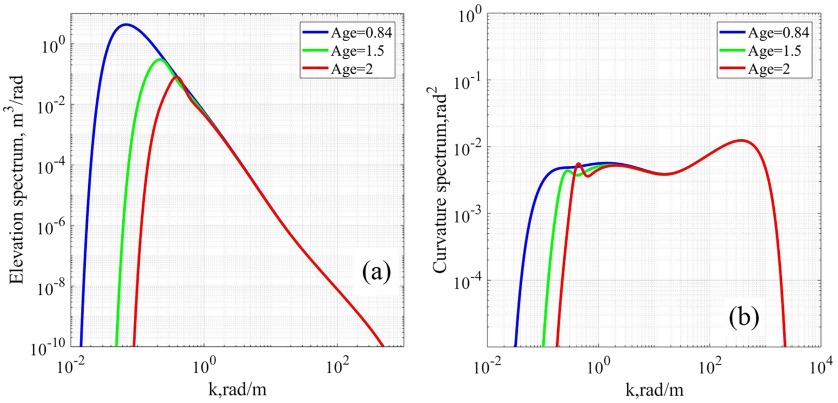

Figure 3. Elevation spectra (a) and curvature spectra (b) of developing waves according to the T. Elfouhaily spectrum model. The wind speed is $U_{10} = 10$ m/s, and the inverse wave ages are $\Omega = 0.84$ (blue curve), 1 (green curve), and 2 (red curve).

Figure 3 shows elevation and curvature spectra of the Elfouhaily spectrum model at a wind speed of $U_{10} = 10$ m/s for various inverse wave ages ($\Omega = 0.84$, 1.5, and 2).

Figure 4 shows the spectra of elevations and spectra of curvatures of the Elfouhaily spectrum model for fully developed waves ($\Omega = 0.84$) and different wind speeds.

It can be seen in Figure 4b that in the range of wave numbers from 1 to 100 rad/m, the spectral density for a higher wind speed can be smaller than the spectral density for a lower wind speed. As it will be shown in section 4 (Figures 14 and 15), this leads to a nonmonotonic dependence of the radar cross section (RCS) on the wind speed.

T. Elfouhaily uses the symmetric spreading function of the form

$$\Phi(k,\varphi) = \frac{1}{2\pi}[1 + \Delta(k)cos(2\varphi)], \tag{18}$$

$$\Delta(k) = \tanh\left\{a_0 + a_p\left(\frac{c}{c_p}\right)^{2.5} + a_m\left(\frac{c_m}{c}\right)^{2.5}\right\}, \tag{19}$$

here $a_0 = \frac{ln(2)}{4}$, $a_p = 4$, and $a_m = 0.13\frac{u_{fr}}{c_m}$. Function (18) is symmetric with respect to $\varphi = \pi/2$, which means the symmetry of crosswind and upwind wave propagation. Such symmetric spectra are obtained by measuring wave slopes with the help of scanning optical wave gauge (Jähne & Riemer, 1990; Keller & Gotwols,

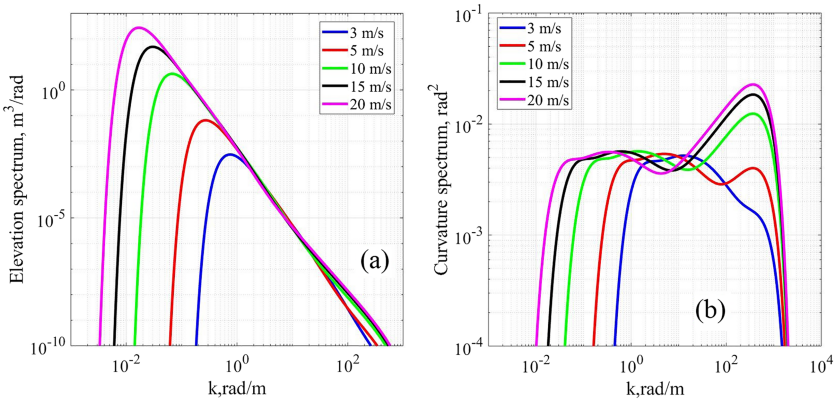

Figure 4. Spectra of elevations (a) and spectra of curvatures (b) of the T. Elfouhaily spectrum model for fully developed waves ($\Omega = 0.84$). The dark blue curve denotes $U_{10} = 3$ m/s, red $U_{10} = 5$ m/s, green $U_{10} = 10$ m/s, black $U_{10} = 15$ m/s, and purple $U_{10} = 20$ m/s.

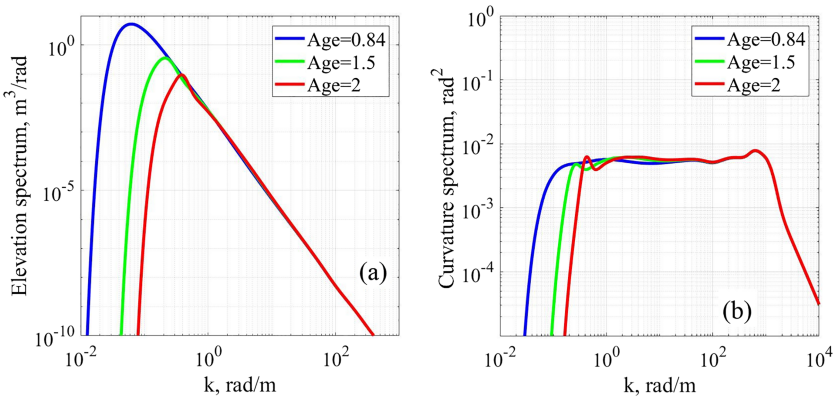

Figure 5. Elevation spectra (a) and the curvature spectra (b) of developing waves according to the V. N. Kudryavtsev spectrum model. The wind is $U_{10} = 10$ m/s, and the wave ages are $\Omega = 0.84$ (blue curve), 1 (green curve), and 2 (red curve).

1983), since the measurement scheme in such systems is capable of measuring only the total spectrum related to the spatial spectrum as follows (Caudal & Hauser, 1996): $\Psi_s(k,\varphi) = \frac{1}{2}(\Psi(k,\varphi) + \Psi(k,\varphi+\pi))$. Therefore, the Elfouhaily spectrum model allows modeling only the total spectrum, rather than the spatial wave spectrum. Accordingly, this model cannot be used to simulate processes in which the direction of the spectrum is important, for example, to calculate the Doppler spectrum of the reflected signal.

Over the last 20 years, the Elfouhaily spectrum has become a kind of classical spectrum and is widely used for simulating surface waves or surface characteristics in the problems where the spatial asymmetry of the wave spectrum is not important. The spectrum model by Elfouhaily et al. (1997) is referred in this paper as Elfouhaily1997.

3.3. V. N. Kudryavtsev Spectrum

V. N. Kudryavtsev used a different approach in his semiempirical spectrum model (Kudryavtsev et al., 1999, 2003, 2005; Appendix A in Yurovskaya et al., 2013). The spatial spectrum of curvatures for short waves is calculated by solving the energy balance equation taking into account the wind effect, resonant nonlinear wave-wave interactions, viscous dissipation, wave breaking, and generation of short waves by longer wave breaking. The equation includes several parameters whose values are chosen by the best fit to the experimental data.

The Kudryavtsev spectrum model proposed in the first papers (Kudryavtsev et al., 1999, 2003) had a gap in the gravity-capillary range (see Fig. 4 in Kudryavtsev et al., 2003). In 2013, the spectrum was improved using new experimental data. Data of a full-scale experiment on stereographic measuring of the two-dimensional spectrum with wavelengths from several millimeters to several centimeters are presented in paper (Yurovskaya et al., 2013). Based on the data of this experiment, the Kudryavtsev spectrum was modified. The measurements were carried out at wind speeds U_{10} from 5 to 15 m/s.

The wind fetch in the wave model is taken into account in the same way as in the Elfouhaily1997 model (see equation (17)). The long-wavelength part of the spectrum is calculated by the model given in Donelan et al. (1985). The transition between long- and short-wavelength parts of the spectrum is described by the same exponential factor as it was in Elfouhaily1997 spectrum (equation (16)). Thus, the spatial spectrum of curvatures is presented as $B(k, \varphi) = B_l(k, \varphi) * F_p + B_h(k, \varphi) * (1 - F_p)$.

The elevation and curvature spectra at a wind speed of $U_{10} = 10$ m/s for various wind fetches ($\Omega = 0.84$, 1.5, and 2) are shown in Figure 5. Figure 6 shows the elevation and curvature spectra of the Kudryavtsev spectrum model for different wind speeds and fully developed waves ($\Omega = 0.84$).

It can be seen in Figure 6b that in the range of wave numbers from 10 to 80 rad/m, the spectral density for a higher wind speed can be smaller than the spectral density for a lower wind speed. As it will be shown in section 4 (Figures 14 and 15), this leads to a nonmonotonic dependence of the RCS on the wind speed. The same effect is observed for the Elfouhaily spectrum due to the fact that both the spectra use the function described by equation (16).

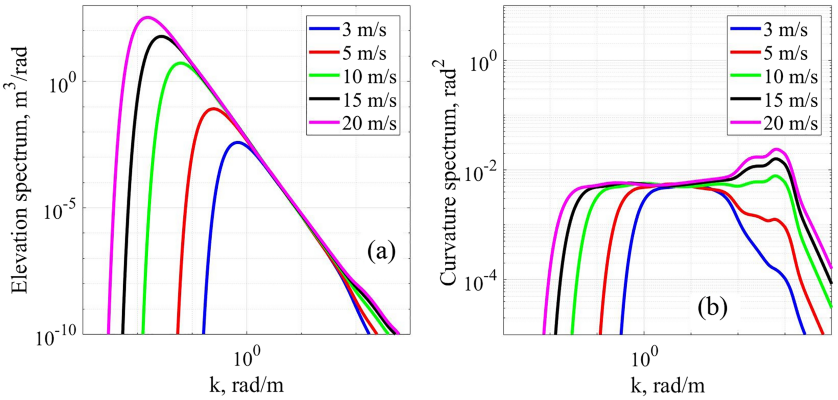

Figure 6. Elevation spectra (a) and the curvature spectra (b) of developing waves according to the V. N. Kudryavtsev spectrum model for fully developed waves ($\Omega = 0.84$). The dark blue curve denotes $U_{10} = 3$ m/s, red $U_{10} = 5$ m/s, green $U_{10} = 10$ m/s, black $U_{10} = 15$ m/s, and purple $U_{10} = 20$ m/s.

The result of solving the energy balance equation is an asymmetric spectrum of surface waves, which shows that downwind propagation of a small ripple is more likely than the upwind one. The long-wavelength spectrum in the paper by Donelan et al. (1985) also has an asymmetric spreading function.

A detailed description of the spectrum can be found in Yurovskaya et al. (2013), Appendix A. In this paper, the numerical code obtained by V. N. Kudryavtsev is used for simulations. The V. N. Kudryavtsev spectrum model is used by many researchers, since it permits one to simulate the influence of various hydrodynamic effects on the spatial wave spectrum. Kudryavtsev's spectrum model (Appendix A in Yurovskaya et al., 2013) is referred below as Kudryavtsev2013.

3.4. P. A. Hwang Spectrum

Based on the parametrization of the wind input source function proposed by Phillips (1984) and on the analysis of experimental data, Hwang and Wang (2004a) described an omnidirectional spectrum of curvatures as the function

$$B(u^*, k) = A(k)\left(\frac{u^*}{c(k)}\right)^{a(k)}, \tag{20}$$

where u^* is the friction velocity and $c(k) = \frac{\omega(k)}{k} = \sqrt{\frac{g}{k} + \frac{T}{\rho}k}$ is the wave phase velocity. The initial approximations of the functions $A(k)$ and $a(k)$ were obtained by analyzing the field experiments on measuring the short-wave spectra by two chains of free-floating wave gauges at wave numbers $1 < k < 300$ rad/m and wind speeds from 2.4 to 14 m/s (Hwang & Wang, 2004a) and are analytically continued for the areas not covered by the measurements (Hwang, 2008). The test procedure is described in Hwang and Wang (2001), Hwang and Wang (2004b), and Wang and Hwang (2004). Figure 7 shows the spectra of elevations and spectra of curvatures of the Hwang spectrum model (Hwang & Fois, 2015a).

The spectrum was refined several times, for example, in Hwang (2010), the spectrum approximation for the upper limit of the wave number was improved. The spectrum modifications based on the analysis of geophysical model functions (GMF), that is, the empirical functions relating the radar backscatter cross section to wind direction and speed, for Ku ($\lambda = 2.1$ cm), C ($\lambda = 5.4$ cm), and L ($\lambda = 23.8$ cm) bands were proposed in Hwang et al. (2013) and Hwang and Fois (2015a, 2015b).

To compare the spectra, we use the version of the spectrum with the corrections proposed in the 2015 paper (Hwang & Fois, 2015a). The 2015 version of the spectrum can be downloaded from the Hwang's (Hwang, 2015) profile on "Researchgate."

The Hwang spectrum has only one parameter, that is, the wind speed, and does not depend on the wind fetch (wave age). The spectrum has two regimes: The first one for moderate wind speeds ($U_{10} < 15$ m/s) mainly relies on experimental data (Hwang & Wang, 2004a), while the second one for high wind speeds

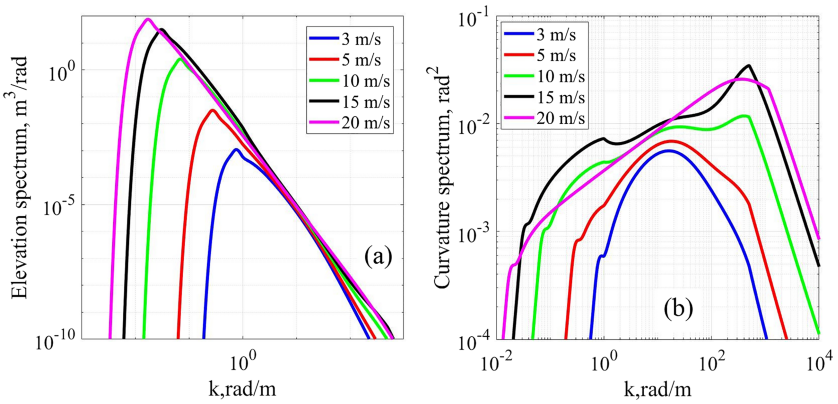

Figure 7. Elevation spectra (a) and the curvature spectra (b) of developing waves according to the P. A. Hwang spectrum model for fully developed waves ($\Omega = 0.84$). The dark blue curve denotes $U_{10} = 3$ m/s, red $U_{10} = 5$ m/s, green $U_{10} = 10$ m/s, black $U_{10} = 15$ m/s, and purple $U_{10} = 20$ m/s.

($15 < U_{10} < 50$ m/s) is based on GMF analytical data (Hwang et al., 2013; Hwang & Fois, 2015a, 2015b). The Hwang model (Hwang & Fois, 2015a) involves the spreading function proposed by Elfouhaily (equation (18).

The Hwang spectrum is useful for simulating radar backscatter cross section for various wavelength ranges of incident radiation and at high wind speeds (up to 50 m/s), which certainly distinguishes it among other models. Hwang's spectrum model (Hwang & Fois, 2015a) is referred below as Hwang2015.

4. Comparison of Models of Spectra

Since there are no experiments on measuring the sea wave spectrum throughout the range of wavelengths that is of interest to specialists in remote sensing, the problem of choosing the most adequate wave spectrum becomes more complicated.

Researchers develop the wave spectrum models, so that they correspond to the problems being solved and to the experimental data. As a result, a large number of models of the surface wave spectrum appeared (e.g., Apel, 1994; Bjerkaas & Riedel, 1979; Bringer et al., 2014; Cheng et al., 2006; Donelan & Pierson, 1987; Elfouhaily et al., 1997; Fois et al., 2014; Hasselmann et al., 1973; Hwang & Fois, 2015a; Kudryavtsev et al., 2003, 2005; Plant, 2002; Toba, 1973; Yurovskaya et al., 2013; Zakharov & Zaslavsky, 1982).

Our aim is to find or develop a spectrum that meets the following criteria:

1. capability of simulating a diverse wave climate;
2. correspondence of the mean square slope (MSS) calculated by the model to the Cox and Munk (1954) experiments and the Bréon and Henriot (2006) results;
3. correspondence of the spreading function to the experimentally measured Doppler spectrum and the MSS from the experiments made by Cox and Munk (1954) and Bréon and Henriot (2006);
4. correspondence of the form of the dependence of the radar backscatter cross section to GMF for various wavelength ranges of incident electromagnetic radiation at moderate incidence angles (20–60°);
5. simplicity of analytical transformations, for example, integration, it can be used for analytical studies of wave spectral properties; and
6. determination of boundary wave numbers for various wavelengths of incident electromagnetic radiation within the framework of a two-scale model of the scattering surface.

4.1. Criteria 1–3

Omnidirectional spectra of elevations and curvatures for the abovementioned models for developed waves ($\tilde{x} = 20{,}170$, $\Omega = 0.84$) at wind speeds of $U_{10} = 3$, 5, 10, 15, and 20 m/s are shown in Figures 2, 4, 6, and 7. Figure 8 shows omnidirectional spectra of elevations and curvatures for developed waves ($\tilde{x} = 20{,}170$, $\Omega = 0.84$) at a wind speed of $U_{10} = 10$ m/s. It can be seen that the elevation spectra for different models are similar, while the spectra of curvatures vary significantly.

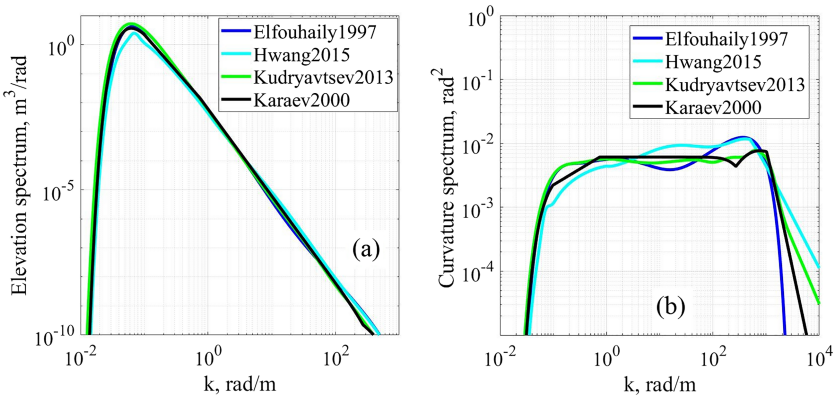

Figure 8. Spectra of elevations (a) and spectra of curvatures (b) for fully developed waves and $U_{10} = 10$ m/s. The dark blue curve is the Elfouhaily1997 spectrum, the light blue one is the Hwang2015 spectrum, the green one is the Kudryavtsev2013 spectrum, and the black curve is the Karaev2000 spectrum.

As already noted, the Hwang2015 spectrum model does not contain a dependence on the wave fetch and thus does not meet Criterion 1.

It is shown in Karaev et al. (2016) that taking into account the wave climate affects the accuracy of the wind speed retrieval from scatterometer data; therefore, the wave spectrum to be used for modeling should include a dependence on the wind fetch.

The measurement of the azimuthal dependence of the Doppler spectrum shows that the angular distribution of waves in the ocean is asymmetric (Plant & Keller, 1990; Poulter et al., 1994) and waves propagate in the downwind direction rather than in the upwind one. Figure 12 in Poulter et al. (1994) shows Doppler spectra measured at various azimuth angles. It is seen that in probing across the direction of wave propagation, in the Doppler spectrum of the reflected radar signal, there are two peaks of approximately the same amplitude, which correspond to sea waves traveling to and from the radar. In probing along the direction of wave propagation only, one peak in the Doppler spectrum is seen. Therefore, for simulating the Doppler spectrum, it is necessary to use a wave spectrum with the corresponding spreading function. Only two spectra among the considered ones have an asymmetric spreading function: the Karaev2000 and Kudryavtsev2013 spectra.

For the Elfouhaily1997 and Kudryavtsev2013 spectra, there is a problem in the range of transition from the low-frequency part to the high-frequency part of the spectrum due to the fact that the spectrum is described as a sum: $B(k,\varphi) = B_l(k,\varphi) * F_p + B_h(k,\varphi) * (1 - F_p)$ (see section 3). It leads to errors in RCS calculations (see Figures 14 and 15). Also, it has reflected on the spreading function in Kudryavtsev2013 spectrum, since the Kudryavtsev2013 two-dimensional spectrum is the result of solving the energy balance equation and the transition function affects both the omnidirectional spectrum and the spreading function.

Figure 9 shows the spreading function of the Elfouhaily1997 spectrum, which is also used in the Hwang2015 spectrum; Figure 10 shows the spreading function of the Kudryavtsev2013 spectrum, and in Figure 11, the spreading function of the Karaev2000 spectrum is shown. The spreading functions are constructed for $k/k_m = 0.5, 1, 5, 10, 50, 100, 500$, and 1,000.

The peculiarities of the spreading function of the Kudryavtsev spectrum for $k/k_m = 5$–100 cause errors in calculating the azimuth dependence of radar backscatter cross section, which will be shown below.

According to the data obtained by Cox and Munk (Cox&Munk1954 on the pictures), the dependence of the MSS on the wind speed is

$$\begin{aligned} \sigma_{up}{}^2 &= 0.00316 \cdot U_{12.5} \pm 0.004, \\ \sigma_{cr}{}^2 &= 0.003 + 0.00192 \cdot U_{12.5} \pm 0.002. \end{aligned} \tag{21}$$

where $\sigma_{up}{}^2$ is the MSS in the upwind direction, $\sigma_{cr}{}^2$ is the MSS in the crosswind direction, $\sigma_t{}^2 = \sigma_{up}{}^2 + \sigma_{cr}{}^2$ is the total MSS, and $U_{12.5}$ is the wind speed at a height of 12.5 m. The Cox and Munk experiments cover the

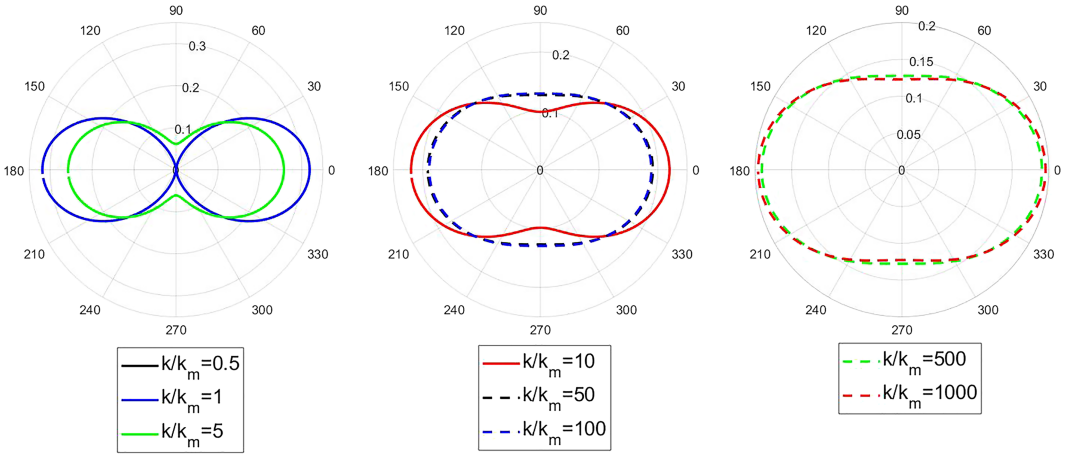

Figure 9. Spreading functions for the Elfouhaily1997 spectrum: (left) The black curve corresponds to $k/k_m = 0.5$, the blue curve is $k/k_m = 1$, and the green one is $k/k_m = 5$; (middle) the red one is $k/k_m = 10$, the black dashed line is $k/k_m = 50$, and the blue dashed line is $k/k_m = 100$; and (right) the green dashed line is $k/k_m = 500$, and the red dashed one is $k/k_m = 1{,}000$.

range of wind speeds from 3 to 14 m/s. In spite of the fact that the experiments were carried out more than half a century ago, dependence (21) is still used to estimate the MSS.

Later optical measurements of the MSS (Bréon & Henriot, 2006; Ross & Dion, 2007) basically confirm their results. For example, as a result of the Bréon and Henriott study, during which 6 million images of the POLDER optical images at a wavelength of 865 nm were analyzed, the following dependences of the MSS on the wind speed at a height of 10 m were obtained

$$\begin{aligned} {\sigma_{\mathrm{up}}}^2 &= 0.001 + 0,00316 \cdot U_{10} \pm 0.00005, \\ {\sigma_{\mathrm{cr}}}^2 &= 0.003 + 0.00185 \cdot U_{10} \pm 0.00005. \end{aligned} \tag{22}$$

Comparison of equations (21) and (22) shows that the Bréon and Henriott results confirm the dependences obtained by Cox and Munk.

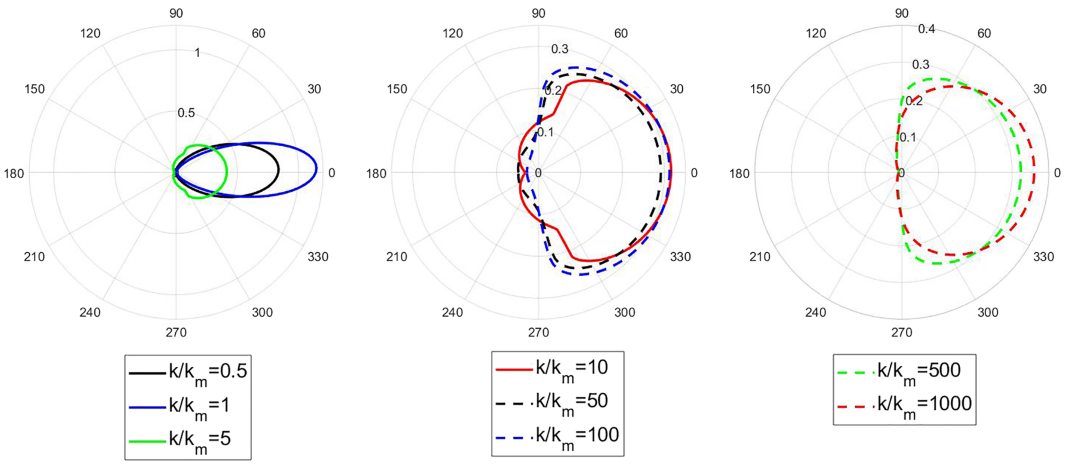

Figure 10. Spreading functions for the Kudryavtsev2013 spectrum: (left) The black curve corresponds to $k/k_m = 0.5$, the blue curve is $k/k_m = 1$, and the green one is $k/k_m = 5$; (middle) the red one is $k/k_m = 10$, the black dashed line is $k/k_m = 50$, and the blue dashed is $k/k_m = 100$; and (right) the green dashed line is $k/k_m = 500$, and the red dashed one is $k/k_m = 1{,}000$.

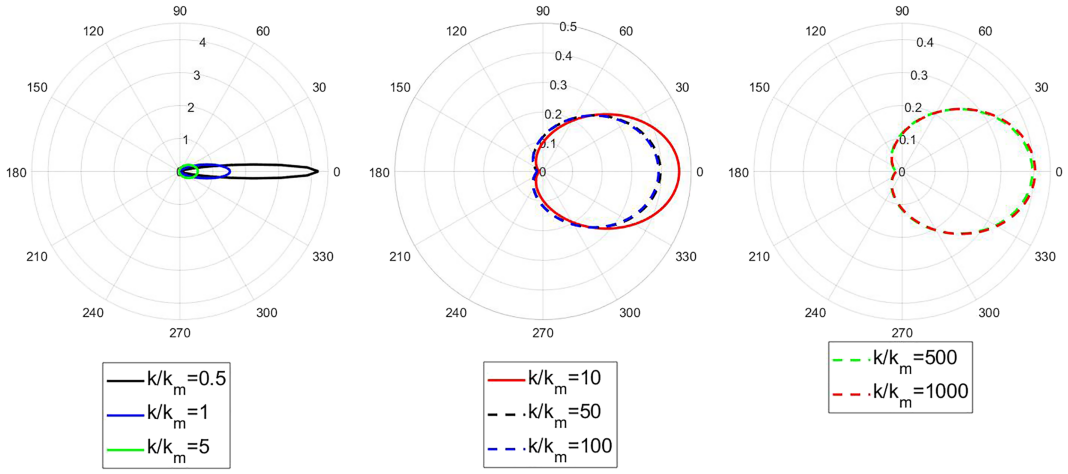

Figure 11. Spreading functions for the Karaev2000 spectrum: (left) The black curve corresponds to $k/k_m = 0.5$, the blue curve is $k/k_m = 1$, and the green one is $k/k_m = 5$; (middle) the red one is $k/k_m = 10$, the black dashed line is $k/k_m = 50$, and the blue dashed line is $k/k_m = 100$; and the green dashed line is $k/k_m = 500$, and the red dashed one is $k/k_m = 1{,}000$.

Equation (21) include the wind speed at a height of 12.5 m. When plotting the graphs, the wind speed at a height of 12.5 m is converted to that at a height of 10 m in the logarithmic profile approximation by the formula (Lamly & Panovskii, 1966):

$$U_{10} = \frac{u^*}{0.4} ln\left(\frac{10}{z_0}\right). \tag{23}$$

The formula is obtained for the case of neutral stratification, where z_0 (in meters) is the surface roughness parameter (elevation). In the calculations, we use the following expression for z_0 (Masuko et al., 1986): $z_0 = \frac{0.000684}{u^*} + 0.428 \cdot (u^*)^2 - 0.0443$, where z_0 and u^* are given in centimeters and centimeters per second, respectively.

The MSS is calculated from the wave spectrum by equations (A8)–(A10). Figure 12 shows the MSS upwind and crosswind calculated by equations (A8) and (A9), respectively, for the following spectrum models: the Karaev2000 model (black curve), the Kudryavtsev2013 model (green curve), the Elfouhaily1997 model (dark blue curve), and the Hwang2015 model (light blue curve). All the calculations are carried out for fully

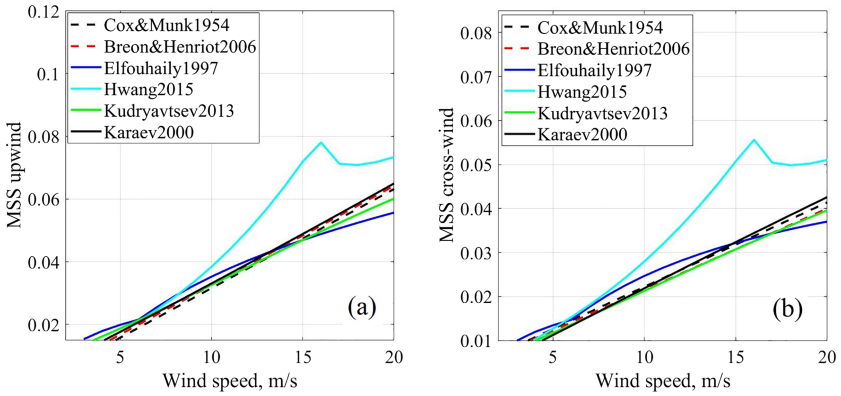

Figure 12. Mean square slope (MSS) upwind (a) and crosswind (b). The black line is the Karaev2000 spectrum, the green one is the Kudryavtsev2013 spectrum, the dark blue curve is the Elfouhaily1997 spectrum, the light blue one is the Hwang2015 spectrum, the black dashed line indicates the experimental dependence obtained by Cox and Munk (1954), and the red one is the dependence obtained by Bréon and Henriot (2006).

developed wind waves. The black dashed line in Figures 12a and 12b shows the MSS obtained from the results of the field experiments made by Cox and Munk (1954), while the Bréon and Henriot (2006) results are indicated in red.

The comparison has shown that the Karaev2000 model (black curve) and the Kudryavtsev2013 model (green curve) provide the best correspondence to the Cox and Munk data and the Bréon and Henriott results.

It is seen in the figure that the Hwang2015 spectrum, when integrated over the entire range of the spectrum specification, substantially disagrees with the experimental data on the MSS. The P. A. Hwang's proposal of solving this problem in his spectrum is discussed in Hwang (2005).

Thus, only two spectra satisfy the Criteria 1–3: the Karaev2000 spectrum and the Kudryavtsev2013 spectrum.

4.2. Criterion 4

The available data of contact measurements of the sea wave spectrum is not enough to determine which of the models best describes real waves. The problem is complex because of the very large dynamic range (more than 100–120 dB), in which accurate measurements are needed. Comparison in integral characteristics, for example, in the MSS, cannot be an unambiguous criterion.

We will try to estimate the short-wavelength part of the wave spectra using, for comparison, the values that directly depend on the ripple spectral density, that is, the radar backscatter cross section for moderate incidence angles.

In the range of moderate incidence angles, the backscattering mechanism is the Bragg (resonant) one, and the scatterer is ripple. The resonant wave number is given by $k_{Br} = 2ksin\theta_0$, where $k = \frac{2\pi}{\lambda}$ is the wave number corresponding to the wavelength of incident radiation λ and θ_0 is the incident angle of radiation.

Within the framework of a two-scale model of the sea surface, the resonant ripple is located on a large wave, which leads to a variation in the local incidence angle along its profile. This results in a so-called tilt modulation, thus to calculate the scattered signal power that is necessary to perform averaging over large-scale wave slopes (related to the local incidence angle).

In a simplified version, the RCS for crosswind probing for a large-scale surface covered with a small ripple can be calculated by the formula (Bass & Fuks, 1979; Born et al., 1979):

$$\sigma_{ij}(\theta) = 4\pi k^4 cos^4\theta \left| g_{ij}(\theta) \right|^2 \cdot [\Psi(2ksin\ \theta, \varphi) + \Psi(2ksin\ \theta, \varphi + \pi)], \tag{24}$$

where the parentheses $\langle\rangle$ denote averaging over the slopes q_x, θ_0 is the probing angle, θ_x is the local incidence angle, that is, $\theta = \theta_0 + \theta_x$ and $q_x = tg\theta_x$, k is the wave number of incident electromagnetic radiation, g_{ij} is the scattering coefficient for the corresponding polarization (Valenzuela, 1978), which depends only on the incidence angle and the dielectric permittivity of the scattering surface, i is the polarization index of incident radiation (V = vertical, H = horizontal), j is the polarization index of scattered radiation (V = vertical, H = horizontal), Ψ is the two-dimensional spectrum of surface waves (A3), and φ is the angle between the probing and wave propagation directions.

The one-dimensional case is presented here. The two-dimensional case is presented in Valenzuela (1978) and similar to one-dimensional case. The presence of large-scale wave slopes leads to an increase in the RCS, since the spectral density of resonant longer waves (due to a variation in the local incidence angle) in the wave spectrum is larger than that of shorter waves. The sea surface slopes distribution is close to normal:

$$P(q_x) = \frac{1}{\sqrt{2\pi\sigma^2_{\text{up}}}} \exp\left(-\frac{{q_x}^2}{2\sigma^2_{\text{up}}} \right). \tag{25}$$

The formula for RCS taking into account tilt modulation is the following:

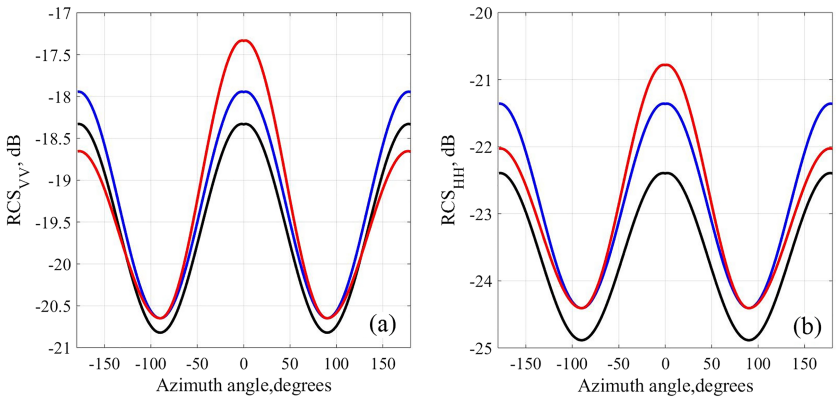

Figure 13. Dependence of the radar backscatter cross section at vertical polarization (a) and at horizontal polarization (b) for the large-scale sea surface covered by a resonance ripple with allowance for hydrodynamic modulation at a wind speed of 10 m/s: The black line is the radar cross section (RCS) for a flat surface covered with ripple. The blue line is the RCS for the large-scale surface covered with a resonant ripple with tilt modulation. The red curve shows the RCS with allowance for hydrodynamic modulation with modulation coefficients of 0.2. The incidence angle is 38.44°.

$$\sigma_{ij}(\theta) = \int_{-\infty}^{\infty} 4\pi k^4 cos^4\theta \left|g_{ij}(\theta)\right|^2 [\Psi(2ksin\ \theta, \varphi) + \Psi(2ksin\ \theta, \varphi + \pi)] P(q_x) \mathrm{d}q_x. \quad (26)$$

Integration to infinite limits in this case does not agree with physics. To obtain a statistically valid estimate of the integration boundary in this calculation, we selected $\left[q_x^{\min}; q_x^{\max}\right] = \left[-3\sqrt{\sigma_{\mathrm{up}}^2}; 3\sqrt{\sigma_{\mathrm{up}}^2}\right]$.

The along-wind slope is gentle than the upwind one, which leads to nonuniform distribution of ripple along the wave profile (Keller & Wright, 1975; Romeiser et al., 1994). The RCS in the along-wind direction is smaller than the upwind RCS due to that fact. This effect is called a hydrodynamic modulation. We take it into account by multiplying spectrum in equation (26) by hydrodynamic modulation coefficient $f(q_x, \varphi)$:

$$\sigma_0(\theta) = \int_{q_x^{\min}}^{q_x^{\max}} 4\pi k^4 cos^4\theta \left|g_{ij}(\theta)\right|^2 [\Psi(2ksin\ \theta, \varphi) + \Psi(2ksin\ \theta, \varphi + \pi)] \cdot f(q_x, \varphi) P(q_x) \mathrm{d}q_x. \quad (27)$$

The following function was used to describe hydrodynamic modulation (Kanevskij & Karaev, 1993):

$$f(q_x, \varphi) = 1 - \beta \cdot q_x sign(cos\ \varphi) cos^2\varphi, \quad (28)$$

where β is modulation coefficient, sign(u) gives the sign of u. In calculations, we assume that $\beta \cdot q_x \leq 0.8$; if $\beta \cdot q_x > 0.8$, then $\beta \cdot q_x = 0.8$.

Figures 13a and 13b give an estimate of the contributions of these modulation mechanisms to the RCS for vertical and horizontal polarizations of radiation within the framework of a two-scale model of the scattering surface (the wavelength is 23.8 cm). The wind speed is $U_{10} = 10$ m/s; the incidence angle is 38.44°. The modified spectrum model described in the following section is used; the case of fully developed waves is studied (dimensionless fetch is 20,170). The black line shows the dependence of the RCS for a flat surface covered with ripple. The blue line shows the dependence of the RCS for a large-scale surface covered with a resonant ripple (tilt modulation) without taking into account hydrodynamic modulation. The red curve shows the dependence with allowance for hydrodynamic modulation coefficient $\beta = 0.2$.

It is seen in the Figure 13 that taking these effects into account can change the RCS by several decibels for vertical polarization. For horizontal polarization, the contribution of these effects is much larger.

To minimize the influence of these effects, one should make estimates under the conditions when the effects of tilt and hydrodynamic modulations are least significant. Therefore, we select vertical polarization which is less sensitive to tilt and hydrodynamic modulations.

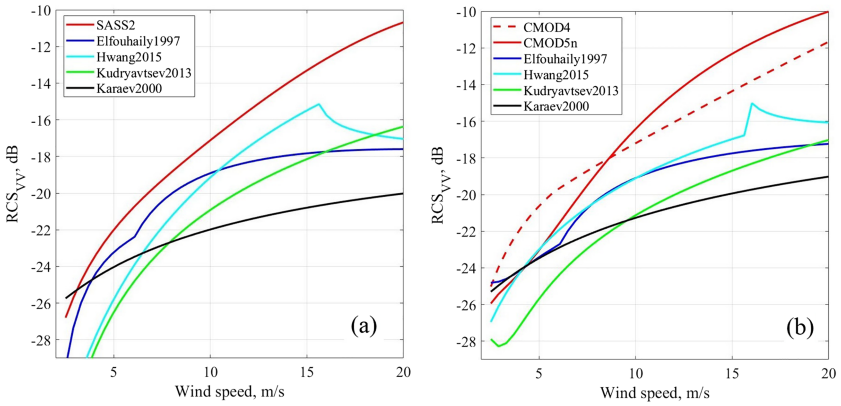

Figure 14. RCS$_{vv}(U_{10})$ for the Ku band (a), the incidence angle is 39.8°, and for the C band (b), the incidence angle is 40°. In both the figures, the black curve is the Karaev2000 spectrum, the green one is the Kudryavtsev2013 spectrum, the dark blue one is the Elfouhaily1997 spectrum, and the light blue one is the Hwang2015 spectrum. In (a), the red curve is SASS2; in (b), the red dashed curve is CMOD4, and the red one is CMOD5n. RCS = radar cross section.

As is seen in the figure, the minimum contribution of large-scale waves (tilt and hydrodynamic modulations) is at an angle of 90° between the probing and wave propagation directions. In this case, the correlation between the spectral density of resonant ripple and the RCS is maximal. Further calculations will be made for vertical polarization and the probing direction of 90°.

The radar backscatter cross section is calculated by the formula

$$\sigma_{ij}(\theta_0) = 4\pi k^4 cos^4\theta_0 \left|g_{ij}(\theta_0)\right|^2 \cdot [\Psi(2ksin\theta_0, \varphi) + \Psi(2ksin\theta_0, \varphi + \pi)]. \quad (29)$$

In contrast to complete formula (24), there is no averaging over slopes and hydrodynamic modulation. In the calculations, we set $\varphi = \frac{\pi}{2}$.

To average over large-scale surface slopes, it is necessary to divide the surface into small-scale and large-scale parts, introduce a boundary wave number, and perform the integration over the wave spectrum to the boundary wave number. However, the concept of the boundary wave number is defined only within the framework of the Karaev2000 spectrum and not defined for the rest of the spectra, thus averaging cannot

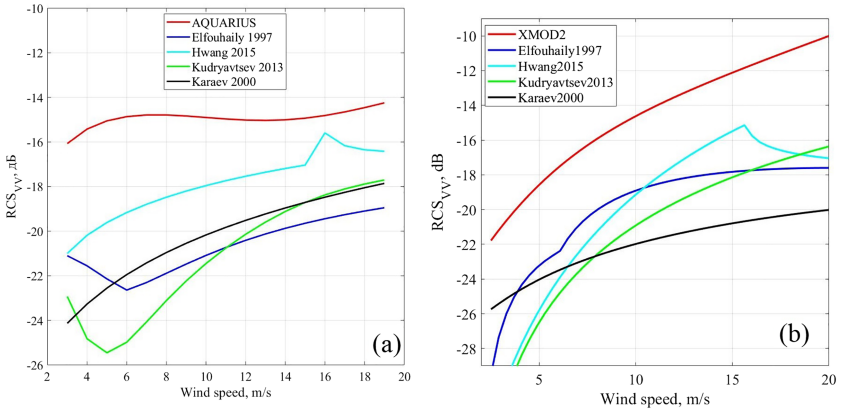

Figure 15. RCS$_{vv}(U_{10})$ for the L band (a), the incidence angle is 38.44°, and X band (b), the incidence angle is 40°. The black curve is the Karaev2000 spectrum, the green one is the Kudryavtsev2013 spectrum, the dark blue one is the Elfouhaily1997 spectrum, and the light blue one is the Hwang2015 spectrum. The red curve in (a) is geophysical model function based o AQUARIUS data. The red curve in (b) is XMOD2. RCS = radar cross section.

be performed in a uniform way. Due to the choice of polarization (vertical) and the probing direction (90°), the modulation effects are minimized, and we compare the models of wave spectra at the resonant ripple wavelength.

We now compare the RCS for the case of vertical polarization of electromagnetic radiation (RCS_{vv}) and the probing direction perpendicular to the wind one, which are calculated by models of wave spectra, with GMF for C (Herbach, 2008; Lecomte, 1993), Ku (Wentz, 1999), X (Li & Lehner, 2014), and L (Meissner et al., 2014) bands.

We are less interested in the absolute correspondence of the RCS_{vv} calculated using the wave spectrum with the GMF, than in the coincidence of the general form of the $RCS_{vv}(U_{10})$ dependence with the GMF on the wind speed.

The fact is that radar equipment developers can achieve stable measurement of the scattered signal power for long-term radar operation, but in spite of all efforts, it is impossible to achieve an exact coincidence in absolute magnitude of the received signal for different radars/scatterometers. Specific test areas, for example, the Amazon forests, are used to perform synchronous measurements with two radars and measure the difference in the RCS. Since this difference is rather stable, the processing algorithms designed for one scatterometer can be applied to another after appropriate correction of the RCS.

Besides, the GMF's coefficients are calculated by regression analysis of the combined data array including scatterometer data (RCS) and sea buoy data (wind speed). As shown in (Elyuocha et al., 2015) using GMFs for the C band, as the scatterometer data array increases, GMFs vary significantly, both in terms of energy characteristics and trends. Figures 2–4 in Elyuocha et al. (2015) show GMFs for the C band. Figures 2 and 3 show the dependence on the wind speed while in Figure 4 is the dependence on the incidence angle. The difference between GMFs can be more than 1 dB.

Therefore, we will not fit the spectrum model to GMFs as it is done in, for example, Bringer et al. (2014) and Fois et al. (2014)) because an error in the GMF on which the model is based can lead to an error in the wave spectrum model. When constructing a wave spectrum model, it is necessary, if possible, to rely on wave measurements using GMFs for control.

The incidence angle is 40° for C band and X band, and it is 39.8° for Ku band and 38.44° for L band. In this case, the Bragg wave number for the Ku band (wavelength = 2.1 cm) is $k_{Br} \approx 384.3$ rad/m, for the C band (wavelength = 5.6 cm) $k_{Br} \approx 147.1$ rad/m, for X band (wavelength = 3.1 cm) $k_{Br} \approx 271$ rad/m, and for L band (wavelength = 23.8 cm) $k_{Br} \approx 32.8$ rad/m. The probing direction is normal to the wind one.

Figure 14a shows the calculated $RCS_{vv}(U_{10})$ dependences for the wind wave models Karaev2000 (black curve), Kudryavtsev2013 (green curve), Elfouhaily1997 (dark blue curve), and Hwang2015 (light blue curve) for the Ku band and the GMF SASS2 (Wentz, 1999). Figure 14b shows similar dependences for the C band and the GMFs CMOD4 (Lecomte, 1993) and CMOD5n (Herbach, 2008). Figure 15a shows the dependences for the L band and the GMF from AQUARIUS measurements (Meissner et al., 2014). Figure 15b shows the dependences for the X band and XMOD2 (Li & Lehner, 2014).

As already mentioned, the features of the Elfouhaily1997 and Kudryavtsev2013 spectra in the range of transition from the high-frequency part of the spectrum to the low-frequency part affect the radar backscatter when calculating RCS in all ranges. At weak winds, the dependence of the radar backscatter cross section on the wind speed becomes ambiguous. This is more valid for the Elfouhaily1997 spectrum than for the Kudryavtsev2013 spectrum, but in both cases, this results in simulation errors leading to errors in wind speed estimation by these models. Thus, for all considered wavelength ranges at middle incidence angles, there is a range of an ambiguous dependence of the RCS on the wind speed for these spectra. The Karaev2000 spectrum does not describe the $RCS(U_{10})$ dependence correctly. The Hwang2015 spectrum has a "kink" at a wind speed of about 15 m/s, when there is a transition from one regime to another. Nevertheless, the general trend of the $RCS_{vv}(U_{10})$ is well reflected using the Hwang and Kudryavtsev spectra.

There are a few GMFs developed for the L band (Meissner et al., 2014; Yueh et al., 2014; Zhou et al., 2016). In all those papers, it was obtained that at wind speeds larger than 8 m/s, there is a normal asymmetry (the upwind RCS is larger than the crosswind one); at smaller wind speeds, there is an abnormal asymmetry (the upwind RCS is smaller than the crosswind one). There is no explanation of this effect. We believe

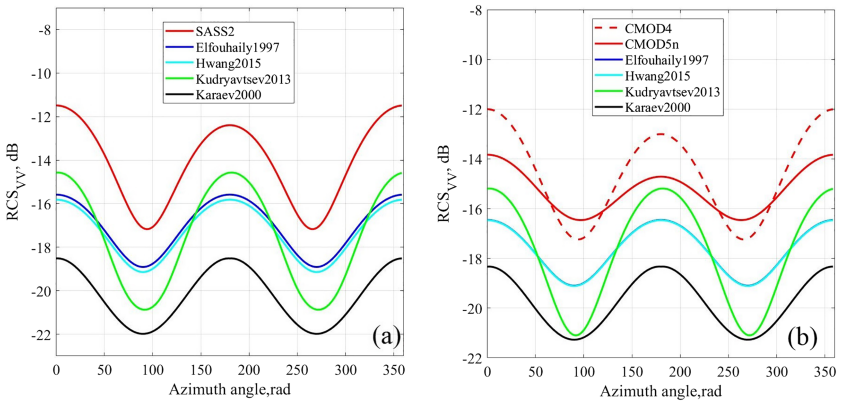

Figure 16. RCS$_{vv}(\varphi)$ for the Ku band (a), the incidence angle is 39.8°, and for the C band (b), the incidence angle is 40°. In both figures, the black curve is the Karaev2000 spectrum, the green one is the Kudryavtsev2013 spectrum, the dark blue one is the Elfouhaily1997 spectrum, and the light blue one is the Hwang2015 spectrum. In (a), the red curve is SASS2; in (b), the red dashed curve is CMOD4, and the red one is CMOD5n. RCS = radar cross section.

that this can be due to the fact that at small wind speeds, waves are weak and can be suppressed by swell with a different angular distribution.

The second test of the wave spectrum models is a comparison with the azimuth dependences of GMF. Figures 16 and 17 show the azimuth dependences of the RCS on the azimuth angle for four wavelength ranges: Ku, C, X, and L bands. The RCS is calculated by the Formula (29). In the calculations, we assume that the wind speed is 10 m/s and the incidence angle is 40° for X and C bands, 39.8° for Ku band, and 38.44° for L band.

The tilt and hydrodynamic modulations were not taken into account in the calculations; thus, there is no difference in the upwind and crosswind backscatter cross sections of radar.

The features of the Kudryavtsev2013 spreading function, which were described in the previous section, lead to errors in the RCS calculation in the L band: The RCS in crosswind probing is larger than that in upwind one. The comparison will be presented in the next section. For other ranges, the Kudryavtsev spectrum gives the overestimated RCS variation as a function of the azimuth angle (the difference between maximum and minimum) compared to the GMF even without averaging over slopes (this will be shown in Table 2). Later, with averaging over slopes, the range of the RCS variation calculated from the Kudryavtsev spectrum will grow, which will further increase the difference between the model and measured RCS(U_{10}) dependences.

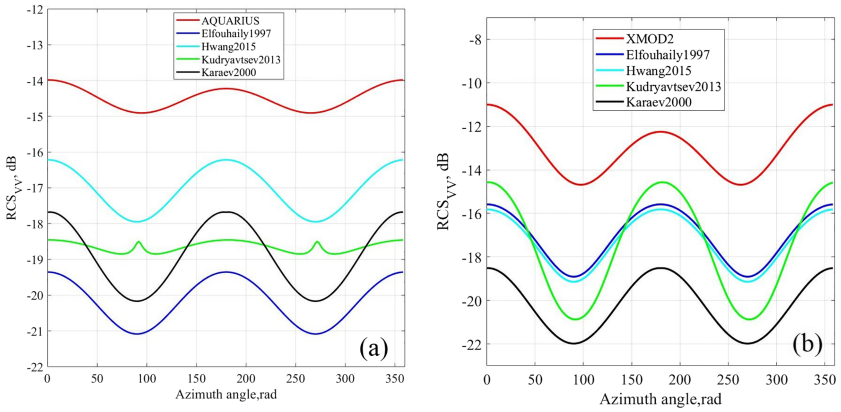

Figure 17. RCS$_{vv}(\varphi)$ for the L band (a), the incidence angle is 38.44°, and X band (b), the incidence angle is 40°. The black curve is the Karaev2000 spectrum, the green one is the Kudryavtsev2013 spectrum, the dark blue one is the Elfouhaily1997 spectrum, and the light blue one is the Hwang2015 spectrum. The red curve in (a) is geophysical model function based o AQUARIUS data. The red curve in (b) is XMOD2. RCS = radar cross section.

Table 1
Criteria for Choosing the Wave Spectrum Model

Criteria	Elfouhaily 1997	Hwang 2015	Kudryavtsev 2013	Karaev 2000
1. Fetch	+	−	+	+
2. Mean square slope	+	−	+	+
3. Spreading function	−	−	−	+
4. Radar cross section	−	+/−	+/−	−
5. Simplicity of formulas	+	+	−	+
6. Division within a two-scale model	−	−	−	+

Therefore, the spreading function of the Karaev2000 spectrum seems to be the best choice among the considered models.

The obtained results allowed tabulating the correspondences of the wave spectrum models to the criteria listed at the very beginning of this section (Table 1).

Thus, none of the considered spectra corresponds to all the criteria defined at the beginning of this section.

The above results have shown that the short-wave part of the Kudryavtsev2013 spectrum model provides a rather good correspondence to the Cox and Munk experiments and rather well describes the dependence of the radar backscatter cross section on the wind speed. The short-wave part of the Kudryavtsev2013 model relies on the measurements from Yurovskaya et al. (2013); therefore, it seems appropriate to refine the Karaev2000 spectrum, which corresponds to most of the criteria using the same experimental data.

5. Modified Spectrum

The modified wind wave spectrum was developed on the basis of the Karaev2000 spectrum model and the experimental results from Yurovskaya et al. (2013). The wave spectrum model is based on the experimental data obtained for wind speeds U_{10} from 5 to 15 m/s. Nevertheless, we extend the range of wind speeds from 3 to 20 m/s to estimate most of the sea surface conditions. For developing wind waves, the dimensionless wind fetch $\tilde{x}$ within the model can vary from 1,430 to 20,170.

5.1. Modified Spectrum: Description

The spectrum (Karaev et al., 2008; Karaev & Balandina, 2000) has shown its validity in the gravity range of the spectrum ($k < 20$ rad/m; Karaev et al., 2002). The spectral range from 10 to 1,000 rad/m is studied in Yurovskaya et al. (2013). Figure 7a in Yurovskaya et al. (2013) shows the spectra of curvatures measured in the experiments on an oceanographic platform near the Katsiveli settlement in the Black Sea (2009–2012). The variation in the relative measurement error (Eq. (9) in Yurovskaya et al., 2013) for the wave number range from 10 to 1,000 rad/m is plotted in Figure 5d in Yurovskaya et al. (2013). It is seen in Figure 5d in Yurovskaya et al. (2013) that the relative error in the range $30 < k < 500$ rad/m (17–119 rad/s) is less than 30%. Based on the analysis of the experimental spectra in this range, the following spectrum modification is proposed (Karaev & Balandina, 2000):

$$S_{\sum}(\omega) = \alpha g^2 \omega^{-5} exp\left\{-1.25\left(\frac{\omega_m}{\omega}\right)^4\right\} \cdot \gamma^{exp\left[-\frac{(\omega-\omega_m)^2}{2\sigma_*^2\omega_m^2}\right]}, 0<\omega<1.2\omega_m, \tag{30a}$$

$$S_{\sum}(\omega) = \frac{\alpha_2}{\omega^4}, \quad 1.2\omega_m<\omega<a_m\omega_m, \tag{30b}$$

$$S_{\sum}(\omega) = \frac{\alpha_3}{\omega^5}, \quad a_m\omega_m<\omega<\omega_{gc1}\approx 20\frac{rad}{s}, \tag{30c}$$

$$S_{\sum}(\omega) = \frac{\alpha_4}{\omega^{n(U_{10})}}, \quad \omega_{gc1}<\omega<\omega_{gc2}\approx 80\frac{rad}{s}, \tag{30d}$$

$$S_{\sum}(\omega) = \frac{\alpha_4}{\omega^{n_1(U_{10})}}, \quad \omega_{gc2}<\omega<\omega_c\approx 500\frac{rad}{s}, \tag{30e}$$

$$S_{\sum}(\omega) = \frac{\alpha_5}{\omega^5}, \quad \omega_c<\omega. \tag{30f}$$

Here $S_{\xi}(\omega)$ is the JONSWAP spectrum (equation (2) in section 2), while the coefficients α_i are calculated as

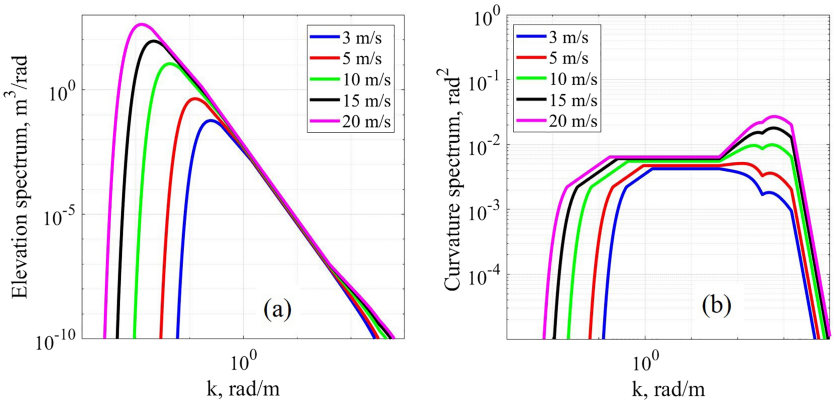

Figure 18. Spectra of elevations (a) and spectra of curvatures (b) of the modified spectrum for fully developed waves ($\tilde{x}$ = 20,170). The dark blue curve denotes U_{10} = 3 m/s, red U_{10} = 5 m/s, green U_{10} = 10 m/s, black U_{10} = 15 m/s, and purple U_{10} = 20 m/s.

$$\alpha_2 = S_{\sum}(1.2\omega_m)\cdot(1.2\omega_m)^4, \tag{31a}$$

$$\alpha_3 = \alpha_2 \cdot a_m \omega_m, \tag{31b}$$

$$\alpha_4 = \alpha_3 \cdot \omega_{gc}^{n(U_{10})-5}, \tag{31c}$$

$$\alpha_5 = \alpha_4 \cdot \omega_{gc}^{n_1(U_{10})-n(U_{10})}, \tag{31d}$$

$$\alpha_6 = \alpha_5 \cdot \omega_c^{5-n_1(U_{10})}. \tag{31e}$$

The coefficients a_m,n,n_1 depend on the wind speed and are given by

$$a_m = 0.8ln(U_{10}) + 1.0, \tag{32a}$$

$$n(U_{10}) = 7.647U_{10}^{-0.237}, \tag{32b}$$

$$n_1(U_{10}) = 0.0007U_{10}^2 - 0.0348U_{10} + 3.271. \tag{32c}$$

The parameters α, γ, and $\widetilde{\omega}_m$ are defined in equation (8a) in section 3. In the range from 20 to 500 rad/s, the spectrum is based on the analysis of the experimental data (Yurovskaya et al., 2013). The elevation spectra of the modified spectrum for wind speeds from 3 to 20 m/s are shown in Figure 18a; the curvature spectra are shown in Figure 18b.

5.2. Modified Spectrum: Comparison

We present the calculation results based on the modified model of the wave spectrum. First of all, we compare the dependences of MSS in the upwind and crosswind directions. The modified spectrum is referred in this paper as Ryabkova2019.

Figure 19 depicts the upwind and crosswind MSS calculated by equations (A8) and (A9), respectively, for the models of the spectra by Karaev2000 (black curve), Kudryavtsev2013 (green curve), and the modified spectrum (purple curve). The black dashed line in Figure 19 denotes the MSS obtained from the results of the full-scale Cox and Munk (Cox & Munk, 1954) experiments and calculated by equation (21). The red dashed line denotes Bréon and Henriot (2006) results (equation (22)). It can be seen that the modified spectrum gives the MSS closer to the experiment than the Kudryavtsev2013 spectrum model due to the gravity range from the model Karaev2000 and the angular distribution (equations (12)–(14)).

We make a comparison for the RCS, since this is the weak point in the Karaev2000 spectrum model. Figures 20 and 21 show the calculated $RCS_{vv}(U_{10})$ dependences for the spectrum models in the C and Ku bands and for L and X bands. Incidence angle is 40° for X and C bands; it is 39.8° for Ku band and 38.44°

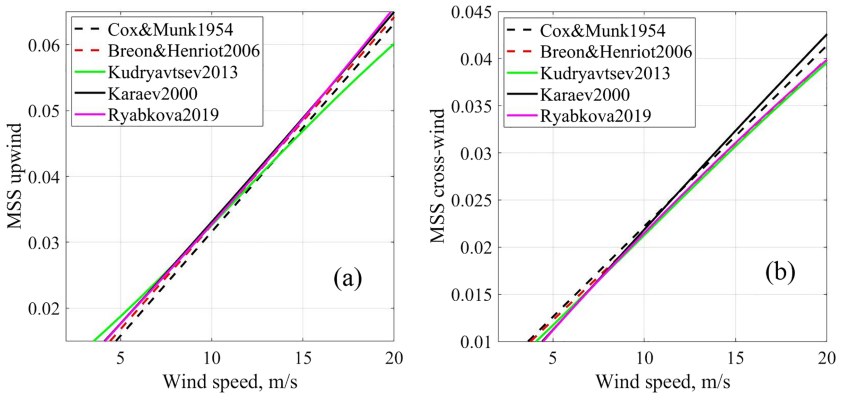

Figure 19. Mean square slope upwind (a) and crosswind directions (b). The black line is the Karaev2000 spectrum, the green one is the Kudryavtsev2013 spectrum, the purple line is the modified spectrum, the black dashed line indicates the experimental dependence obtained by Cox and Munk (1954), and the red one is the dependence obtained by Bréon and Henriot (2006).

for L band. The probing is normal to the wind direction. Figures 22 and 23 show the calculated $RCS_{vv}(\varphi)$ for different ranges at the same incidence angles and the wind speed $U_{10} = 10$ m/s.

Table 2 shows the difference between the RCS in upwind and crosswind directions for GMFs and spectra models. In Figures 21 and 22, one can see that for the Hwang2015 spectrum model, there is always a "kink" near 15 m/s, which results from the difference between the regimes at moderate and high wind speeds. For the Elfouhaily1997 spectrum model, there is always a kink as well, but near 8 m/s, we believe that it can be explained by the fact that for wave numbers larger than 0.1 rad/m, there is a "mix-up" in the elevation and curvature spectra: The spectrum corresponding to a higher wind speed is lower than the spectrum for a lower wind speed. The kink in the RCS for the Kudryavtsev2013 spectrum model can be explained by the same effect. It happens due to the fact that both Elfouhaily1997 and Kudryavtsev2013 use the same function to describe the transition between high and low wave number parts of the spectrum (equation (16)). Elfouhaily1997 uses this function only for omnidirectional spectra, while the spreading function is the same for all wave numbers that is why the dependence of the RCS on the azimuth angle does not have any kink. Kudryavtsev2013 uses different spreading functions for different wavelengths, which leads to errors in the RCS for the L band (see Figure 23a). We think the modeled RCS should be unambiguous to be used, for example, for developing wind speed retrieval algorithms. It is seen in Figures 20–23 and in Table 2 that the modified spectrum does not provide an ideal correspondence to the GMF, but it models the trend

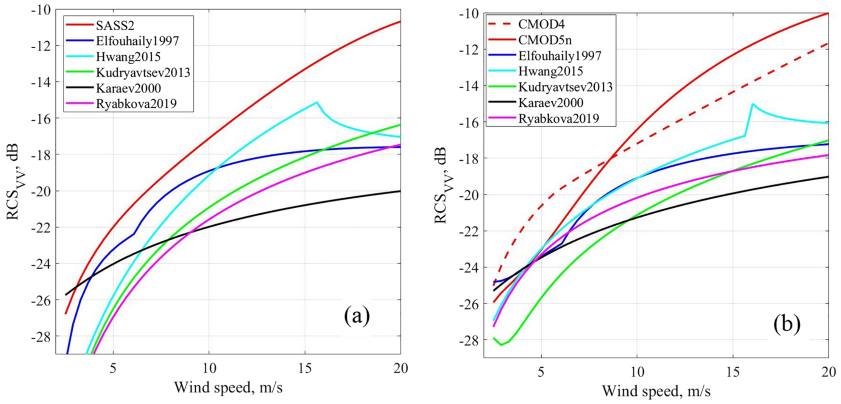

Figure 20. $RCS_{vv}(U_{10})$ for the Ku band (a), the incidence angle is 39.8°, and for the C band (b), the incidence angle is 40°. The black curve is the Karaev2000 spectrum, the green curve is the Kudryavtsev2013 spectrum, the dark blue one is the Elfouhaily1997 spectrum, the light blue one is the Hwang2015 spectrum, the purple curve is the modified spectrum, and the red curve is the geophysical model function for the corresponding wavelength. RCS = radar cross section.

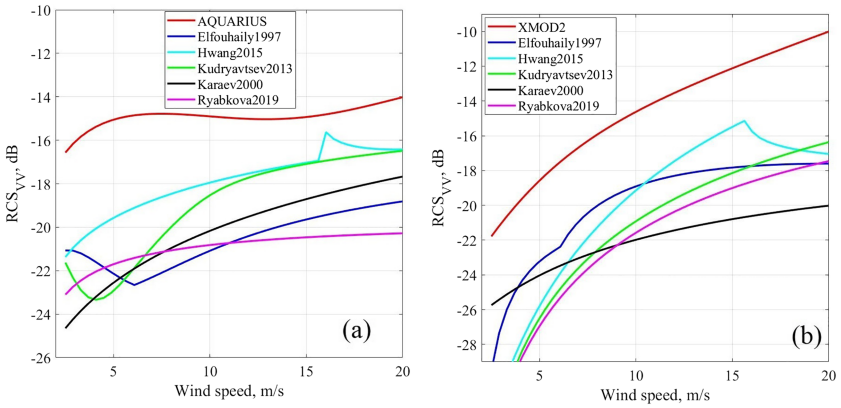

Figure 21. RCS$_{vv}$(U_{10}) for the L band (a), the incidence angle is 38.44°, and X band (b), the incidence angle is 40°. The black curve is the Karaev2000 spectrum, the green curve is the Kudryavtsev2013 spectrum, the dark blue one is the Elfouhaily1997 spectrum, the light blue one is the Hwang2015 spectrum, the purple curve is the modified spectrum, and the red curve is the geophysical model function for the corresponding wavelength. RCS = radar cross section.

correctly, and it is free of any kinks. The modeled RCS was calculated for the "pure Bragg scattering" without tilt or hydrodynamic modulations that may add a few decibels to the RCS (equation (29)).

It is seen that for the modified spectrum, the coincidence with GMFs is improved compared to the previous version of the spectrum (Karaev & Balandina, 2000). The modified spectrum allows the improvement of the modeling of the RCS and can be used to simulate surface waves in the gravity-capillary range of the spectrum.

The next step in the development of the wave spectrum model is to simplify its application within the framework of a two-scale model of the scattering surface.

5.3. Modified Spectrum: Boundary Wave Numbers

Within the framework of a two-scale model of sea surface, waves are divided into two parts: large-scale and small-scale waves. The division criterion is known (Bass & Fuks, 1979): The ratio of the incident radiation wavelength to the curvature radius of large-scale waves should be much less than unity:

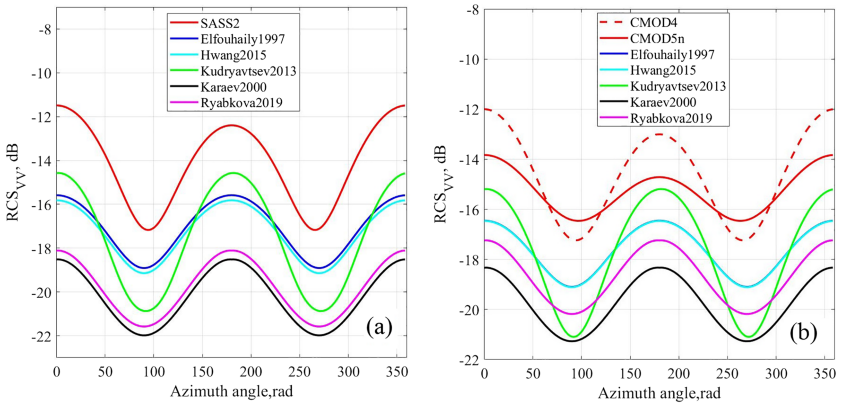

Figure 22. RCS$_{vv}$(φ) for the Ku band (a), the incidence angle is 39.8°, and for the C band (b), the incidence angle is 40°. The black curve is the Karaev2000 spectrum, the green curve is the Kudryavtsev2013 spectrum, the dark blue one is the Elfouhaily1997 spectrum, the light blue one is the Hwang2015 spectrum, the purple curve is the modified spectrum, and the red curve is the geophysical model function for the corresponding wavelength. RCS = radar cross section.

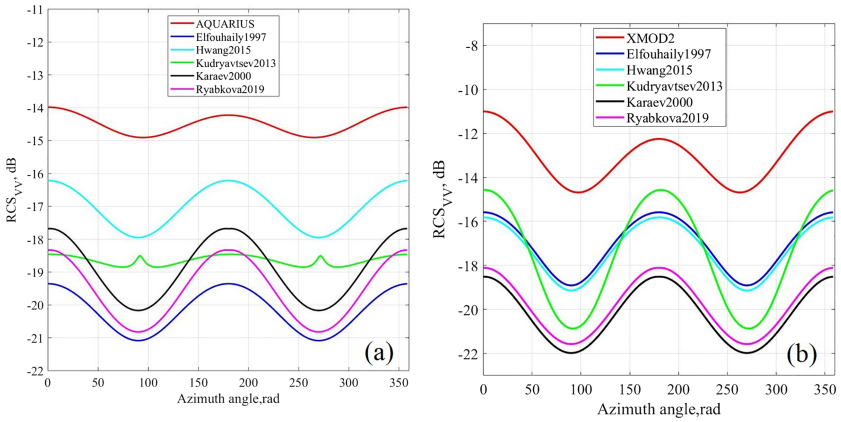

Figure 23. $RCS_{vv}(\varphi)$ for the L band (a), the incidence angle is 38.44°, and X band (b), the incidence angle is 40°. The black curve is the Karaev2000 spectrum, the green curve is the Kudryavtsev2013 spectrum, the dark blue one is the Elfouhaily1997 spectrum, the light blue one is the Hwang2015 spectrum, the purple curve is the modified spectrum, and the red curve is the geophysical model function for the corresponding wavelength. RCS = radar cross section.

$$\sqrt[3]{\left(\frac{\lambda}{2\pi}\frac{1}{R}\right)}\frac{1}{cos\theta_0}\ll 1, \tag{33}$$

where $\frac{1}{R^2}=\int_0^{k_b}k^4S(k)\mathrm{d}k$, k_b is a boundary wave number and θ_0 is an incidence angle. However, the meaning of "much less than unity" is not defined.

The MSSs of large-scale waves in Ku and Ka bands were measured when analyzing the data of Dual-frequency Precipitation Radar and buoy data (Panfilova & Karaev, 2016). Fully developed wind waves were considered. On the other hand, the total MSS of large-scale waves can be calculated from the wave spectrum by the formula

$$\sigma_t^2=\int_0^{k_b}k^2S(k)\mathrm{d}k, \tag{34}$$

here $S(k)$ is omnidirectional wave spectrum ((A2)). Knowing the MSS of large-scale waves, we can determine the boundary wave number for the Ku band.

There are no measurements of the MSS of large-scale waves in C, X, and L bands, that is, the above approach is not applicable and a different approach is proposed. We determine the boundary wave number for the Ku and Ka bands and find the condition for curvature smallness. The condition of smallness depends on the peak wave number. For Ku- and Ka-bands and for θ_0= 0–10° ($cos\theta_0$ is considered to be equal 1 for $0^\circ<\theta_0<10^\circ$), the division criterion between large and small waves (in terms of a two-scale model) is

$$\sqrt[3]{\left(\frac{\lambda}{2\pi}\frac{1}{R}\right)}=2.6376\cdot k_m^2-0.9241\cdot k_m+0.3437, \tag{35}$$

here $k_m=\omega_m^2/g$, ω_m is calculated using ((3b)) and ((8a)). We assume that this is a universal smallness

Table 2
RCS_{vv} (0)-RCS_{vv} (π/2) for Spectra and GMFs (dB)

Bands	Elfouhaily 1997	Hwang 2015	Kudryavtsev 2013	Karaev 2000	Ryabkova 2019	GMF
Ku	3.30	3.30	6.21	3.52	3.52	5.96 (SASS2)
X	3.26	3.26	6.51	3.28	3.28	3.6 (XMOD2)
C	2.73	2.73	6.13	2.97	2.97	5.55 (CMOD4); 1.80 (CMOD5n)
L	1.73	1.73	0.09	2.49	2.49	0.91 (AQUARIUS)

Note. GMF = geophysical model function.

criterion and use it for other electromagnetic wavelengths. As a result, we obtain the dependence of the boundary wave number on the peak wave number; therefore, these formulas may be applied for developing wind waves also. The dependences of boundary wave numbers on the peak wave number for θ_0= 0–10° for the bands are as follows:for the Ku band (2.2 cm)

$$k_b = 68.126886 + 72.806451 \cdot k_m + 12.93215 \cdot k_m^2 \cdot ln(k_m) - 0.39611989 \cdot \frac{ln(k_m)}{k_m} - \frac{0.42195392}{k_m},$$

for the C band (5.6 cm)

$$k_b = 2.7367946 - 2.2640513 \cdot k_m + 15.497567 \cdot \sqrt{k_m} + \frac{1.7039154}{\sqrt{k_m}} - 0.0009902319 \cdot \frac{ln(k_m)}{k_m^2},$$

for the X band (3.1 cm)

$$k_b = 25.817117 + 25.425253 \cdot k_m - 16.426717 \cdot k_m \cdot ln(k_m) + \frac{1.9827813}{\sqrt{k_m}} + \frac{0.099565741}{k_m^{\frac{3}{2}}},$$

for the L band (23.8 cm)

$$k_b = 0.72021748 + 2.5587343 \cdot k_m - 1.1346396 \cdot k_m^{\frac{3}{5}} + \frac{0.0067571611 \cdot ln(k_m)}{k_m} + \frac{0.0059406387}{k_m^{\frac{3}{5}}},$$

and for the Ka band (0.8 cm)

$$k_b = 24833 \cdot k_m^2 - 2624.9 \cdot k_m + 570.9.$$

The dependences of the wave number of the incidence radiation ($k_{inc} = \frac{2\pi}{\lambda_{inc}}$) to the boundary wave numbers ratio on the peak wave number for θ_0= 0–10° for the bands are as follows:for the Ku band (2.2 cm)

$$\frac{k_{inc}}{k_b} = \frac{-0.28772736 + 201.154 \cdot k_m + 5029.3442 \cdot k_m^2 - 1084.0284 \cdot k_m^3 - 508.2843 \cdot k_m^4}{1 + 51.599988 \cdot k_m + 1226.2775 \cdot k_m^2 + 946.45102 \cdot k_m^3 - 425.83084 \cdot k_m^4},$$

for the C band (5.6 cm)

$$\frac{k_{inc}}{k_b} = 87.175187 + 112.10344 \cdot k_m - 79.291411 \cdot \sqrt{k_m} \cdot ln(k_m) - 152.90596 \cdot \sqrt{k_m} - 109.55633 \cdot e^{k_m},$$

for the X band (3.1 cm)

$$\frac{k_{inc}}{k_b} = \frac{-1.4741293 + 331.62483 \cdot k_m + 661.8967 \cdot k_m^2}{1 + 48.325056 \cdot k_m + 200.92632 \cdot k_m^2 + 12.384079 \cdot k_m^3},$$

for the L band (23.8 cm)

$$\frac{k_{inc}}{k_b} = 122.08408 - 109.36945 \cdot k_m + 98.430374 \cdot \sqrt{k_m} \cdot ln(k_m) - \frac{1.2950102}{k_m} + \frac{0.006541626}{k_m^2},$$

and for the Ka band (0.8 cm)

$$\frac{k_{inc}}{k_b} = \frac{1}{0.72689246 - 3.3421265 \cdot k_m + 31.618358 \cdot k_m^2}.$$

Figure 24a shows the dependences of the boundary wave number on the peak wave number for θ_0= 0–10° for Ku, Ka, C, X, and L bands. Figure 24b shows the dependences of the wave number of the incidence radiation to the boundary wave number ratio on the peak wave number for θ_0= 0–10° for Ku, Ka, C, X, and L bands.

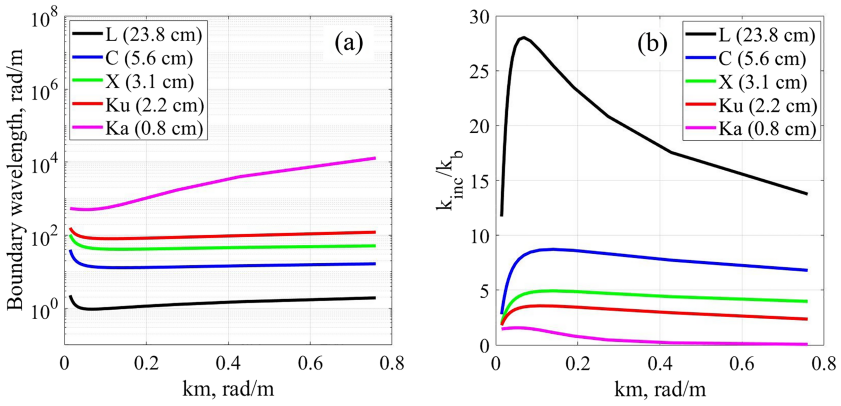

Figure 24. The dependences of the boundary wave number on the peak wave number (left plot); the dependences of the wave number of the incidence radiation to the boundary wave number ratio on the peak wave number (right plot). θ_0= 0–10°; red curve denotes Ku band, purple curve Ka band, blue curve C band, green curve X band, and black curve L band.

Equation (35) is valid for incidence angles close to zero (<10°), because the dependences of the MSS on the wind speed for Ku and Ka bands from Panfilova and Karaev (2016) were obtained from the Dual-frequency Precipitation Radar data, its incidence angles are in the range 0–17°. The variation of boundary wave numbers on the incidence angle is a topic for another research.

It is seen from Figure 24 that boundary wave number for Ka band is not consistent with boundary wave number for other ranges. It happened due to the fact that incidence radiation of the Ka range (0.8 cm) corresponds to wave number 785 rad/m, while the spectrum measurements by Yurovskaya et al. (2013) for wave numbers larger than 500 rad/m have relative error (Eq. (9) in the paper) larger than 40%. The capillary spectrum measurements are required for correct approximation of the high-frequency part of the spectrum.

Note that except for the range near the peak, the spectrum has a power law form $S(\omega)$~ω^n, which simplifies analytical transformations and the study of the contribution of a particular spectral range to various integral characteristics.

6. Swell

The proposed wind wave spectrum enables to model developing wind waves and fully developed wind waves that correspond to the case of a dimensionless wind fetch more than 20,170. If the wind speed has decreased or wind has changed its direction, swell begins to form.

In result, the most frequent sea state is the mixed sea. In this case we observe the sea surface wind waves and swell.

A simple spectrum model of gentle swell is described by the formula (Neumann, 1952):

$$S_{\text{swell}}(\omega) = 6m_0\left(\frac{\omega_m}{\omega}\right)^5\omega^{-1}exp\left\{-1.2\left(\frac{\omega_m}{\omega}\right)^5\right\}, \tag{36}$$

where m_0 is the first moment of the wave spectrum, that is, the significant wave height (SWH) is $SWH = 4\sqrt{m_0}$. The significant wave height of swell reduces in propagation. There is a maximum value of m_0 for every ω_m (dominant wavelength L_m), it determines the upper limit of the swell height. The simplest formula to estimate this value is $S_{\text{swell}}(\omega_m) = S_{\sum}(\omega_m)$, where $S(\omega)$ is the spectrum for the fully developed wind waves. Thus m_0 is calculated as follows: $m_0 = \frac{\alpha\gamma g^2 e^{-0.05}}{6\omega_m^4}$,and the SWH maximum for swell of the dominant wavelength L_m is equal to

$$SWH = 4\frac{ge^{-0.025}}{\omega_m^2}\sqrt{\frac{\alpha\gamma}{6}}.$$

Therefore, we can simulate mixed seas by presenting their spectra as the sum of wind waves and swell: $S(\omega) = S_{\sum}(\omega)+S_{swell}(\omega)$.

We know ω_m and k_m of wind waves and the SWH of swell. Swell has the same ω_m as the initial wind wave. By varying the SWH of swell from the SWH of the initial wind wave (initial stage) to 0 (final stage), we obtain swell of the required intensity.

7. Conclusions

Numerical simulation of sea waves is actively used to study the microwave electromagnetic wave scattering from the sea surface and to solve inverse problems, that is, to determine the wave parameters and the surface wind speed from remote sensing data. Numerical experiments enable one to study the features of the scattered radar signal in a wide range of conditions that often cannot be established in the experiment. The accuracy of modeling largely depends on the quality of the employed wave spectrum model.

At the beginning of the 1990s, wave spectrum models applicable for modeling were developed by oceanographers, for example, the spectrum by Donelan et al. (1985). However, the application of the wave spectrum models in radar problems has shown that they have a number of significant drawbacks, which stimulated the development of spectrum models focused on remote sensing problems, for example, the Elfouhaily spectrum. Some drawbacks were eliminated in new wave spectrum models, and then these models were used to simulate the energy characteristics of a scattered radar signal (radar backscatter cross section).

However, in modeling scatterometers and assessing the accuracy of algorithms for determining the surface wind speed, GMF were used (Karaev et al., 2013; Karaev et al., 2015). The GMF yield an unambiguous relationship between the wind speed and the backscatter radar cross section, which is in contrary to fact. Studies have shown that the degree of wave development has a strong impact on the accuracy of the surface wind speed retrieval from altimeter and scatterometer data (e.g., Karaev et al., 2002; Karaev et al., 2016).

To study this effect by numerical simulation, one should use a wave spectrum model. The requirements to the wave spectrum model were formulated, and the correspondences of the most popular wave spectrum models to these requirements were analyzed. The available models do not meet these requirements in full and are not capable of providing a realistic simulation of the effect of the wave climate on the precise determination of the surface wind speed.

To solve the problem, the available wave spectrum model (Karaev, 2000) was modified on the basis of new data. In the experiment on the offshore platform installed in the Black Sea, the short-wave part of the wave spectrum was measured (Yurovskaya et al., 2013).

As a result of the study, a modified wave spectrum model has been developed, which meets all the requirements for the numerical modeling of scatterometer measurements to estimate the effect of wave parameters and the degree of wave development on the accuracy of the algorithm for the wind speed retrieval.

Oil slick influences the spectral density of short waves; therefore, the sea wave spectrum model with improved part of resonant ripple opens new possibility for numerical simulation of oil slicks.

For the convenience of using the modified wave spectrum model, the boundary wave number dependences were calculated, which, in accordance with a two-scale model of the scattering surface, divide the wave spectrum into large-scale and small-scale components.

Except for the range near the peak, the formula for the modified wave spectrum model has a simple analytical form, which is convenient for transformation and numerical simulation.

Swell is added to the model, so it can be used for mixed sea modeling.

Appendix A: Terminology

The frequency spectrum $S_{\sum}(\omega)$ and the frequency-angular spectrum $\Psi(\omega,\varphi) = S_{\sum}(\omega)\Phi_{\omega}(\omega,\varphi)$ are usually used in oceanography to describe surface waves, where $S_{\sum}(\omega)$ is the frequency distribution of the wave energy, $\Phi_{\omega}(\omega,\varphi)$ is the spreading function, and φ is the azimuth angle measured from the wind direction axis.

The transition from the frequency-angular wave spectrum to the spatial spectrum of the wave numbers $\Psi(k,\varphi)$ is performed taking into account the dispersion relation; in all the spectra considered in this paper, the dispersion relation for gravity-capillary waves in deep water is used ($kH \gg 1$,H is the depth):

$$\omega^2 = gk\left(1 + \frac{T}{g\rho}k^2\right), \tag{A1}$$

where T is the coefficient of water surface tension, ρ is the water density, and g is the acceleration due to gravity. The coefficients T and ρ depend on the observation conditions. In the calculations, we accept $T = 0.0074$ H/m, $\rho = 1{,}000$ kg/m^3, and $g = 9.81$ m/s^2.

The relation between omnidirectional and directional elevation spectra is

$$S(k) = \int_{-\pi}^{\pi} \Psi(k,\varphi) k d\varphi. \tag{A2}$$

The directional elevation spectrum is given by

$$\Psi(k,\varphi) = \frac{1}{k} S(k) \Phi(k,\varphi) = \Psi\left(k_x, k_y\right), \tag{A3}$$

where the spreading function is

$$\Phi(k,\varphi) = \frac{k\Psi(k,\varphi)}{\int_{-\pi}^{\pi} k\Psi(k,\varphi) d\varphi}, \tag{A4}$$

with the normalization condition imposed on it

$$\int_{-\pi}^{\pi} \Phi(k,\varphi) \mathrm{d}\varphi = 1. \tag{A5}$$

The directional curvature spectrum can be determined as

$$X(k,\varphi) = k^4 \Psi(k,\varphi), \tag{A6}$$

the omnidirectional curvature (saturation) spectrum is

$$B(k) = k^3 S(k). \tag{A7}$$

The upwind MSS is determined as

$$\sigma_{\mathrm{up}}{}^2 = \int_{-\infty}^{\infty}\int_{-\pi}^{\pi} k^2 cos^2\varphi \Psi(k,\varphi) k \mathrm{d}k \mathrm{d}\varphi, \tag{A8}$$

and the crosswind MSS is

$$\sigma_{\mathrm{cr}}{}^2 = \int_{-\infty}^{\infty}\int_{-\pi}^{\pi} k^2 sin^2\varphi \Psi(k,\varphi) k \mathrm{d}k \mathrm{d}\varphi. \tag{A9}$$

The total MSS has the form

$$\sigma_t^2 = \sigma_{\mathrm{up}}{}^2 + \sigma_{\mathrm{cr}}{}^2 = \int_{-\infty}^{\infty}\int_{-\pi}^{\pi} k^2 \Psi(k,\varphi) k \mathrm{d}k \mathrm{d}\varphi. \tag{A10}$$

More detailed derivation of formulas is given in Elfouhaily et al. (1997) and Holthuijsen (2007).

The wide frequency range of the sea wave spectrum can be divided into several ranges. It is generally accepted that waves of a length of more than 7 cm ($k \approx 90$ rad/m, $\omega \approx 30$ rad/s) refer to gravity ones, waves of a length from 0.6 cm ($k \approx 1{,}050$ rad/m, $\omega \approx 310$ rad/s) to 7 cm to gravity-capillary ones, and waves of a length of less than 0.6 cm to capillary ones (Davidan et al., 1985). The boundary between the ranges is conventional, since it depends on the quantitative determination of the criterion of smallness of the surface tension effect on the dispersion relation.

Acknowledgments
This work was supported by the Bureau of International Cooperation, Chinese Academy of Sciences, the Chinese-foreign cooperation in key projects "The detection of oil spill and its ecological impact study" (133337KYSB20160002) and supported in part by the National Natural Science Foundation of China (41576032) and the Russian Foundation for Basic Research (project "Development of new methods for radar sensing of inland waters and coastal areas"; 17-05-00939). The authors express their gratitude to Maria Yurovskaya for the wave spectra data and to Vladimir Kudryavtsev for the numerical code of his spectrum and fruitful discussions. The data needed to understand and build upon the published research is provided in Ryabkova (2019).

References

Alves, J. H. G. M., Banner, M. L., & Young, I. R. (2003). Revisiting the Pierson-Moskowitz asymptotic limits for fully-developed wind waves. *Journal of Physical Oceanography*, *33*(7), 1301–1323. https://doi.org/10.1175/1520-0485(2003)033<1301:RTPALF>2.0.CO;2

Apel, J. R. (1994). An improved model of the ocean surface wave vector spectrum and its effects on radar backscatter. *Journal of Geophysical Research*, *99*(C8), 16,269–16,291. https://doi.org/10.1029/94JC00846

Babanin, A. V., & Soloviev, Y. V. (1998). Field investigation of transformation of the wind wave frequency spectrum with fetch and the stage of development. *Journal of Physical Oceanography*, *28*(4), 563–576. https://doi.org/10.1175/1520-0485(1998)028<0563:fiotot>2.0.co;2

Banner, M. L. (1990). Equilibrium spectra of wind waves. *Journal of Physical Oceanography*, *20*(7), 966–984. https://doi.org/10.1175/1520-0485(1990)020<0966:esoww>2.0.co;2

Bass, F. G., & Fuks, I. M. (1979). *Wave scattering from statistically rough surfaces*. Oxford, UK: Pergamon Press.

Bjerkaas, A.W., & Riedel, F.W. (1979). Proposed model for the elevation spectrum of a wind-roughened sea surface (Technical Report APL-TG-1328-1-3). Laurel, Md: Applied Physics Laboratory, Johns Hopkins University.

Born, G. H., Dunne, J. A., & Lame, D. B. (1979). Seasat mission overview. *Science*, *204*(4400), 1405–1406. https://doi.org/10.1126/science.204.4400.1405

Bréon, F. M., & Henriot, N. (2006). Spaceborne observations of ocean glint reflectance and modeling of wave slope distributions. *Journal of Geophysical Research*, *111*, C06005. https://doi.org/10.1029/2005JC003343

Bringer, A., Chapron, B., Mouche, A., & Guérin, C.-A. (2014). Revisiting the short-wave spectrum of the sea surface in the light of the weighted curvature approximation. *IEEE Transactions on Geoscience and Remote Sensing*, *52*(1), 679–689. https://doi.org/10.1109/TGRS.2013.2243459

Caudal, G., & Hauser, D. (1996). Directional spreading function of the sea wave spectrum at short scale, inferred from multifrequency radar observations. *Journal of Geophysical Research*, *101*(C7), 16,601–16,613. https://doi.org/10.1029/96JC00921

Cheng, Y., Liu, Y., & Xu, Q. (2006). A new wind-wave spectrum model for deep water. *Indian Journal of Marine Sciences*, *35*(3), 181–194.

Cox, C. S., & Munk, W. H. (1954). Statistics of the sea surface derived from Sun glitter. *Journal of Marine Research*, *13*, 198–227.

Davidan, I. N. (1983). Some results of studying the wind wave spectrum at very small fetches (in Russian). *Proceedings of the State Oceanographic Institute*, *169*, 17–30.

Davidan, I. N., Lopatuhin, L. I., & Rozhkov, V. A. (1985). *Wind waves in the world ocean (in Russian)*. Leningrad: Gidrometizdat.

Donelan, M. A., Hamilton, J., & Hui, W. H. (1985). Directional spectra of wind generated waves. *Philosophical Transactions of the Royal Society A: Mathematical, Physical and Engineering Sciences*, *315*(1534), 509–562. https://doi.org/10.1098/rsta.1985.0054

Donelan, M. A., & Pierson, W. J. Jr. (1987). Radar scattering and equilibrium ranges in wind-generated waves with application to scatterometry. *Journal of Geophysical Research*, *92*(C5), 4971–5029. https://doi.org/10.1029/JC092ic05p04971

Elfouhaily, T., Chapron, B., Katsaros, K., & Vandemark, D. (1997). A unified directional spectrum for long and short wind-driven waves. *Journal of Geophysical Research*, *102*(C7), 15,781–15,796. https://doi.org/10.1029/97JC00467

Elyuocha, A., Neyt, H., Stoffelen, A., & Verspeek, J. (2015). Assessment of the corrected CMOD6 GMF using scatterometer data. Paper presented at SPIE Remote Sensing of the Ocean, Sea Ice, Coastal Waters, and Large Water Regions 2015, Toulouse, France. https://doi.org/10.1117/12.2195727

Ewing, J. A. (1980). Observations of wind-waves and swell at an exposed coastal location. *Estuarine and Coastal Marine Science*, *10*(5), 543–554. https://doi.org/10.1016/s0302-3524(80)80074-0

Fois, F., Hoogeboom, P., Le Chevalier, F., & Stoffelen, A. (2014). An investigation on sea surface wave spectra and approximate scattering theories. Paper presented at IEEE Geoscience and Remote Sensing Symposium 2014, Quebec City, Canada. https://doi.org/10.1109/IGARSS.2014.6947457

Hasselmann, K., Barnett, T. P., Bouws, E., Carlson, H., Cartwright, D. E., Enke, K., et al. (1973). Measurements of wind-wave growth and swell decay during the Joint North Sea Wave Project (JONSWAP). *Deutches Hydrographisches Zeitschr*, *A8*(12), 1–95.

Herbach, H. (2008). CMOD5.N: A C-band geophysical model function for equivalent neutral wind. In *European centre for Medium-Range Weather Forecast Technical Memoranda* (Vol. 554, pp. 1–20). Shinfield Park, Reading, UK: ECMWF. https://doi.org/10.21957/mzcfm6jfl

Holthuijsen, L. H. (2007). *Waves in oceanic and coastal waters*. New York: Cambridge University press.

Hwang, P. (2015). Ocean surface roughness spectrum matlab code package (H15 version). https://doi.org/10.13140/RG.2.1.4272.9689

Hwang, P. A. (2005). Wavenumber spectrum and mean square slope of intermediate-scale ocean surface waves. *Journal of Geophysical Research*, *110*, C10029. https://doi.org/10.1029/2005JC003002

Hwang, P. A. (2008). Observations of swell influence on ocean surface roughness. *Journal of Geophysical Research*, *113*, C12024. https://doi.org/10.1029/2008JC005075

Hwang, P. A. (2010). A Note on the ocean surface roughness spectrum. *Journal of Atmospheric and Oceanic Technology*, *28*(3), 436–443. https://doi.org/10.1175/2010jtecho812.1

Hwang, P. A., Atakturk, S., Sletten, A., & Trizna, D. B. (1996). A study of the wavenumber spectra of short water waves in the ocean. *Journal of Physical Oceanography*, *26*(7), 1266–1285. https://doi.org/10.1175/1520-0485(1996)026<1266:asotws>2.0.co;2

Hwang, P. A., Burrage, D. M., Wang, D. W., & Wesson, J. C. (2013). Ocean surface roughness spectrum in high wind condition for microwave backscatter and emission computations. *Journal of Atmospheric and Oceanic Technology*, *30*(9), 2168–2188. https://doi.org/10.1175/jtech-d-12-00239.1

Hwang, P. A., & Fois, F. (2015a). Surface roughness and breaking wave properties retrieved from polarimetric microwave radar backscattering. *Journal of Geophysical Research: Oceans*, *120*, 3640–3657. https://doi.org/10.1002/2015JC010782

Hwang, P. A., & Fois, F. (2015b). Inferring surface roughness and breaking wave properties from polarimetric radar backscattering. Paper presented at IEEE International Geoscience and Remote Sensing Symposium 2015, Milan, Italy. https://doi.org/10.1109/IGARSS.2015.7326326.

Hwang, P. A., & Wang, D. W. (2001). Directional distributions and mean square slopes in the equilibrium and saturation ranges of the wave spectrum. *Journal of Physical Oceanography*, *31*(5), 1346–1360. https://doi.org/10.1175/1520-0485(2001)031<1346:ddamss>2.0.co;2

Hwang, P. A., & Wang, D. W. (2004a). An empirical investigation of source term balance of small scale surface waves. *Geophysical Research Letters*, *31*, L15301. https://doi.org/10.1029/2004GL020080

Hwang, P. A., & Wang, D. W. (2004b). Field measurements of duration limited growth of wind-generated ocean surface waves at young stage of development. *Journal of Physical Oceanography*, *34*(10), 2316–2326. https://doi.org/10.1175/1520-0485(2004)034<2316:fmodgo>2.0.co;2

Jähne, B., & Riemer, K. S. (1990). Two-dimensional wave number spectra of small-scale water surface waves. *Journal of Geophysical Research*, *95*(C7), 11,531–11,546. https://doi.org/10.1029/JC095ic07p11531

Kahma, K. (1981). A study of the growth of the wave spectrum with fetch. *Journal of Physical Oceanography*, *11*(11), 1503–1515. https://doi.org/10.1175/1520-0485(1981)011<1503:asotgo>2.0.co;2

Kanevskij, M. B., & Karaev, V. Y. (1993). Spectrum of a radar signal backscattered from sea surface (in Russian). *Izvestiya VUZ. Radiofizika*, *36*(1), 3–15.

Kanevsky, M. B. (2017). *How the radar with synthesized aperture sees the ocean surface (in Russian)*. Nizhny Novgorod: Federal Research Center, Institute of Applied Physics of the Russian Academy of Sciencies.
Karaev, V., Kanevsky, M., & Meshkov, E. (2008). The effect of sea surface slicks on the Doppler spectrum width of a backscattered microwave signal. *Sensors*, *8*, 3780–3801.
Karaev, V., Meshkov, E., Shlaferov, A., & Kuznetsov, Yu. (2013). Russian scatterometer METEOR-3: A review of the first numerical simulations. Paper presented at International Geoscience and Remote Sensing Symposium 2013, Melburne, Australia.
Karaev, V. Y., & Balandina, G. N. (2000). A modified wave spectrum and remote sensing of ocean (in Russian). *Issledovanie Zemli is kosmosa*, *5*, 45–56.
Karaev, V. Y., Balandina, G. N., & Angelov, M. K. (1998). *On the features of wave description as applied to solving problems of remote sensing of the sea surface: Preprint No. 470 (in Russian)*. Nizhny Novgorod: Federal Research Center, Institute of Applied Physics of the Russian Academy of Sciencies.
Karaev, V. Y., Kanevsky, M. B., Balandina, G. N., Kotton, P. D., Challenor, P. G., Gommenginger, C. P., & Srokosz, M. A. (2002). On the problem of the near ocean surface wind speed retrieval by radar altimeter: A two-parameter algorithm. *International Journal of Remote Sensing*, *23*(16), 3263–3283. https://doi.org/10.1080/01431160110075587
Karaev, V. Y., Panfilova, M. A., & Jie, G. (2016). The effect of the wave type on the backscatter cross section in the range of middle incidence angles (in Russian). *Izvestiya, Atmospheric and Oceanic Physics*, 1–2.
Karaev, V. Y., Panfilova, M. A., Titchenko, Y. A., Meshkov, E. M., Balandina, G. N., Kuznetsov, Y. V., & Shlaferov, A. L. (2015). Russian scatterometer: Discussion of the concept. *International Journal of Remote Sensing*, *36*(24), 6056–6084. https://doi.org/10.1080/01431161.2015.1110637
Keller, W. C., & Gotwols, B. L. (1983). Two-dimensional optical measurement of wave slope. *Applied Optics*, *22*(22), 3476–3478. https://doi.org/10.1364/ao.22.003476
Keller, W. C., & Wright, J. W. (1975). Microwave scattering and the straining of wind-generated waves. *Radio Science*, *10*, 139–147.
Kitaigorodskii, S. A. (1962). Applications of the theory of similarity to the analysis of wind-generated wave motion as a stochastic process. *Izvestiya Akademii Nauk SSSR. Seria Geofizicheskaya*, *1*, 105–117. English Edition, 73-80
Kitaigorodskii, S. A., Krasitskii, V. P., & Zaslavskii, M. M. (1975). On Phillips Theory of equilibrium range in the spectra of wind-generated gravity waves. *Journal of Physical Oceanography*, *13*(5), 816–827.
Klinke, J., & Jähne, B. (1992). 2D wave number spectra of short wind waves-Results from wind wave facilities and extrapolation to the ocean. In *Optics of the Air-Sea Interface: Theory and Measurement* (Vol. 1749, pp. 245–257). Bellingham, Washington USA: Society of Photo Optical. https://doi.org/10.1117/12.138853
Kudryavtsev, V., Akimov, D., Johannessen, J., & Chapron, B. (2005). On radar imaging of current features: 1. Model and comparison with observations. *Journal of Geophysical Research*, *110*, C07016. https://doi.org/10.1029/2004JC002505
Kudryavtsev, V., Hauser, D., Caudal, G., & Chapron, B. (2003). A semiempirical model of the normalized radar cross-section of the sea surface. 1. Background model. *Journal of Geophysical Research*, *108*(C3), 8054. https://doi.org/10.1029/2001JC001003
Kudryavtsev, V., Makin, D., & Chapron, B. (1999). Coupled sea surface-atmosphere model. 2 Spectrum of short wind waves. *Journal of Geophysical Research*, *104*(C4), 7625–7639. https://doi.org/10.1029/1999JC900005
Lamly J. L., & Panovskii, G. A. (1966). *Structure of atmospheric turbulence*. (in Russian). Moskow: Mir.
Lecomte, P. (1993). CMOD4 model description. Version 1.2. ER-TN-ESA-GP-1120
Li, X.-M., & Lehner, S. (2014). Algorithm for sea surface wind retrieval from TerraSAR-X and TanDEM-X data. *IEEE Transactions on Geoscience and Remote Sensing*, *52*(5), 2928–2939. https://doi.org/10.1109/TGRS.2013.2267780
Liu, P. C. (1989). On the slope of the equilibrium range in the frequency spectrum of wind waves. *Journal of Geophysical Research*, *94*(C4), 5017–5023. https://doi.org/10.1029/JC094ic04p05017
Masuko, H., Okamoto, K., Shimada, M., & Niwa, S. (1986). Measurement of microwave backscattering signatures of the ocean surface using X band and Ka band airborne scatterometers. *Journal of Geophysical Research*, *91*(C11), 13,065–13,083. https://doi.org/10.1029/JC091ic11p13065
Meissner, T., Wentz, F. J., & Ricciardulli, L. (2014). The emission and scattering of L-band microwave radiation from rough ocean surfaces and wind speed measurements from the Aquarius sensor. *Journal of Geophysical Research:. Oceans*, *119*, 6499–6522. https://doi.org/10.1002/2014JC009837
Neumann, G. (1952). On ocean wave spectra and a new method of forecasting wind-generated sea. *Beach Erosion Board, U. S. Army Corps of Engineers, Tech. Memo* 43, 1-42.
Panfilova, M.A. & Karaev, V.Y. (2016). Evaluation of the boundary wave number for the two-scale model of backscatter of microwaves in Ka- and Ku-band by the sea surface using the Dual-frequency Precipitation Radar data, Paper presented at IEEE International Geoscience and Remote Sensing Symposium 2016, Beijing, China. https://doi.org/10.1109/IGARSS.2016.7729956
Phillips, O. M. (1958). The equilibrium range in the spectrum of wind-generated waves. *Journal of Fluid Mechanics*, *4*(04), 426–434.
Phillips, O. M. (1984). On the response of short ocean components. *Journal of Physical Oceanography*, *14*, 1425–1433.
Phillips, O. M. (1985). Spectral and statistical properties of the equilibrium range in wind-generated gravity waves. *Journal of Fluid Mechanics*, *156*, 505–531. https://doi.org/10.1017/S0022112085002221
Pierson, W. J. Jr., & Moskowitz, L. A. (1964). Proposed spectral form for fully developed wind seas *based* on the similarity theory of S.A. Kitaigorodskii. *Journal of Geophysical Research*, *69*(25), 5181–5190.
Plant, W. J. (2002). A stochastic, multiscale model of microwave backscatter from the ocean. *Journal of Geophysical Research*, *107*(C9), 3120. https://doi.org/10.1029/2001JC000909
Plant, W. J. (2009). The ocean wave height variance spectrum: Wavenumber peak versus frequency peak. *Journal of Physical Oceanography*, *39*(9), 2382–2383. https://doi.org/10.1175/2009jpo4268.1
Plant, W. J., & Keller, W. C. (1990). Evidence of Bragg scattering in microwave Doppler spectra of the sea return. *Journal of Geophysical Research*, *95*(C9), 16,299–16,310. https://doi.org/10.1029/JC095ic09p16299
Poulter, E. M., Smith, M. J., & McGregor, J. A. (1994). Microwave backscatter from the sea surface: Bragg scattering by short gravity waves. *Journal of Geophysical Research*, *99*(C4), 7929–7943. https://doi.org/10.1029/93JC03562
Rodrigues, G., & Soares, C. G. (1999). Uncertainty in the estimation of the slope of the high frequency tail of wave spectra. *Applied Ocean research*, *21*(4), 207–213. https://doi.org/10.1016/s0141-1187(99)00014-0
Romeiser, R., Schmidt, A., & Alpers, W. (1994). A three-scale composite surface model for the ocean wave-radar modulation transfer function. *Journal of Geophysical Research*, *99*(C5), 9785–9801.
Ross, V., & Dion, D. (2007). Sea surface slope statistics derived from sun glitter radiance measurements and their apparent dependence on sensor elevation. *Journal of Geophysical Research*, *112*, C09015. https://doi.org/10.1029/2007JC004137

Ryabkova, M. (2019). Data for a review of wave spectrum models as applied to the problem of radar probing of the sea surface in JGR: Oceans. *Ver. 3 (Version 1)*. figshare. https://doi.org/10.6084/m9.figshare.9747662.v1

Toba, Y. (1973). Local balance in the air-sea boundary process. *Journal of the Oceanographic Society of Japan*, *29*(5), 209–225. https://doi.org/10.1007/BF02108528

Valenzuela, G. R. (1978). Theories for the interaction of electromagnetic and oceanic waves—A review. *Boundary-Layer Meteorology*, *13*, 61–85. https://doi.org/10.1007/BF00913863

Wang, D. W., & Hwang, P. A. (2004). On the dispersion relation of short gravity waves from space-time wave measurements. *Journal of Atmospheric and Oceanic Technology*, *21*, 1936–1945.

Wentz, F. J. (1999). A model function for the ocean-normalized radar cross section at 14 GHz derived from NSCAT observations. *Journal of Geophysical Research*, *104*(C5), 11,499–11,514.

Young, I. R. (1999). *Wind-generated ocean waves*, *Elsevier ocean engineering book series* (Vol. 2). Oxford, UK: Elsevier.

Yueh, S. H., Tang, W., Fore, A. G., Hayashi, A. K., Song, Y. T., & Lagerloef, G. (2014). Aquarius geophysical model function and combined active passive algorithm for ocean surface salinity and wind retrieval. *Journal of Geophysical Research: Oceans*, *119*, 5360–5379. https://doi.org/10.1002/2014JC009939

Yurovskaya, M. V., Dulov, V. A., Chapron, B., & Kudryavtsev, V. N. (2013). Directional short wind wave spectra derived from the sea surface photography. *Journal of Geophysical Research: Oceans*, *118*, 1–15. https://doi.org/10.1002/jgrc.20296

Zakharov, V. E., & Badulin, S. I. (2015). The generalized Phillips' spectra and new dissipation function for wind-driven seas, 1-16. arXiv:1212.0963v2 [physics.ao-ph]

Zakharov, V. E., & Filonenko, N. N. (1996). Energy spectrum for stochastic oscillations of the surface of a liquid. *Dokl. Akad. Nauk SSSR*, *170*(6), 1292–1295.

Zakharov, V. E., & Zaslavsky, M. M. (1982). Kinetic equation and Kolmogorov spectra in weak- turbulent theory of wind waves. *Izvestiya, Atmospheric and Oceanic Physics*, *18*(9), 970–980.

Zhou, X., Chong, J., Yang, X., Li, W., & Guo, X. (2016). Ocean surface wind retrieval using SMAP L-band SAR. *IEEE Journal of Selected Topics in Applied Earth Observations and Remote Sensing*, *10*(1), 65–74. https://doi.org/10.1109/jstars.2016.2630919